journal of the mechanical behavior of biomedical materials 137 (2023) 105533

Contents lists available at ScienceDirect

Journal of the Mechanical Behavior of Biomedical Materials

journal homepage: www.elsevier.com/locate/jmbbm

Corrosion and wear behavior of Ti–5Cu-xNb biomedical alloy in simulated body fluid for dental implant applications

Anurag Kumar Pandey [a], R.K. Gautam [a,*], C.K. Behera [b]

[a] Department of Mechanical Engineering, Indian Institute of Technology (Banaras Hindu University) Varanasi, Varanasi- 221005, India
[b] Department of Metallurgical Engineering, Indian Institute of Technology (Banaras Hindu University) Varanasi, Varanasi- 221005, India

ARTICLE INFO

Keywords:
Ti–Cu–Nb ternary Alloy
Corrosion
Tribological study
SBF
Dental implant application

ABSTRACT

The present study examined the corrosion and tribological behavior of novel Ti–5Cu-xNb alloy synthesized via powder metallurgy as a new biomedical material in a simulated bodily fluid (SBF) solution. The electrochemical impedance spectroscopy (EIS) study reveals the formation of two protective layers on the surface of alloys during the test. The alloys spontaneously produce a passivating oxide coating on their surfaces, and the breakdown potential (1.14–1.17 V) and re-passivation current density (2.07–3.04 μAcm^{-2}) were observed during the potentiodynamic polarization test. The highest corrosion resistance was observed for the alloy Ti–5Cu–10Nb (i_{corr} = 21.44 nA-cm^{-2}). The SEM and XPS analysis of the corroded surface showed the formation of oxide on the surfaces of the alloys. The samples were tested at 10 N, 15 N, and 20 N loads against the zirconia counterpart to investigate the effect of loading on friction and wear. The lowest coefficient of friction was obtained for Ti–5Cu–5Nb (0.25–0.41) at 20 N loading, while the maximum for Ti–5Cu–10Nb at 15 N load falls in the range of (0.71–0.25). Additionally, they present the wear rate in the range of (5.3×10^{-8}-1.45×10^{-6} mm^3/mm), in accordance with the change in microstructure and mechanical properties. However, the wear rate increases with the addition of niobium and reaches the maximum for Ti–5Cu–15Nb at 20 N loading condition, but it is relatively deficient compared to commonly used implant material. Therefore, it is suggested that this β-type Ti–5Cu-xNb alloy is a promising candidate, more suitable than the commercially used Ti and Ti–6Al–4V for dental applications.

1. Introduction

Commercial applications of titanium and titanium alloys have been steadily increasing in recent decades due to their remarkable corrosion resistance and high specific strength. Commercially pure Ti lacks optimal mechanical behavior, limiting its application in various applications, particularly where great mechanical strength is required (Geetha et al., 2009). To increase the mechanical strength, many elements are added during processing to stabilize the phases of titanium alloy. Titanium exhibits two phases below 882 °C of its hexagonal closed pack structure (α); above this, it is body-centered cubic (β). Both stages have a unique properties. However, the combined α+β phase of titanium is better suited for orthopedic and dentistry (Mitsuo, 1998; Taddei et al., 2004). Ti–6Al–4V is an excellent example of the combined phase, which offers lower elastic modulus and better corrosion strength. Still, due to several disadvantages related to neurological disorders and Alzheimer's diseases caused by V and Al, researchers focus on Al and V-free α+β titanium alloys to use in dentistry (Elias et al., 2015). Copper is an essential element of the body because of its good antibacterial and antimicrobial properties (Liu et al., 2014; Tao et al., 2020). Numerous studies have been published on the growth of *S. aureus* and *E. coli* bacteria near the dental implant periphery, creating etching and swelling and finally loosening the implant in the future (Barth et al., 1989; Liu et al., 2008). Bacterial infections induced by indwelling devices are widespread and challenging to treat due to the need for long-term antibiotic therapy and costly surgical procedures, which can impose high financial costs on patients (Khan et al., 2008; Sohail et al., 2011). As a result, in addition to using antibiotics during surgery, another option to limit the risk of infection is to design novel implants with antibacterial properties. Antibacterial rudiments (Cu^{2+}, Ag^{+}, and Zn^{2+}) have been incorporated into titanium and titanium alloys to generate antibacterial properties (Szaraniec and Goryczka, 2017; X. Wang et al., 2019) and good cytocompatibility (Gao et al., 2019). Copper will be one of the utmost favorable elements in medical applications because of its low

* Corresponding author.
E-mail addresses: anuragkrpandey.rs.mec17@itbhu.ac.in (A.K. Pandey), rkg.mec@itbhu.ac.in (R.K. Gautam), ckbehera.met@itbhu.ac.in (C.K. Behera).

https://doi.org/10.1016/j.jmbbm.2022.105533
Received 20 July 2022; Received in revised form 13 October 2022; Accepted 16 October 2022
Available online 27 October 2022
1751-6161/

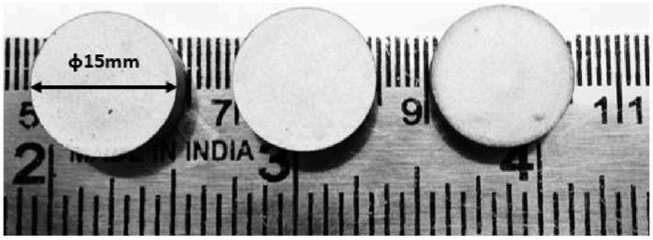

Fig. 1. Image of the alloy after it has been sintered.

Table 1
Chemical composition of the reagents in 1000 mL simulated body fluid.

Reagents	Amount in 1000 mL
NaCl	8.035 g
$NaHCO_3$	0.355 g
KCl	0.225 g
$MgCl_2.6H_2O$	0.311 g
Na_2SO_4	0.072 g
1.0M HCl	39 mL
$CaCl_2$	0.292 g
$((HOCH_2)_3CNH_2)$	6.118 g

cost, high antibacterial efficiency, low cytotoxicity, and stable reactivity (Heidenau et al., 2005; Zhang et al., 2018). However, adding copper enhances the implant's mechanical strength, corrosion resistance, and antibacterial ability, but excess copper also deteriorates the anticorrosive ability, antibacterial property, and ductility (Cao et al., 2012; Taira et al., 1989).

Additionally, by attaching to sulfate or carboxylate-containing groups in proteins or enzymes, Cu ions may change their structure or function (Thurman and Gerba, 1989). They may also promote the harmful action of superoxide radicals and result in "multiple hit damage" at specific places (Samuni et al., 1984; Sterritt and Lester, 1980). Previous research showed that adding 5% Cu is sufficient to enhance the corrosion resistance and antibacterial property of the cPTi and Ti–6Al–4V surgical implant (Liu et al., 2014; Ren, Ling, zheng ma, 2014). Heat treatment also affects the property of Ti–Cu alloy (Zhang et al., 2016), showed that the formation of the Ti_2Cu phase on the surface showed strong solid strengthening ability and the critical factor for excellent antibacterial ability. The main phases which formed with the addition of copper are α-Ti + Ti_2Cu, α-Ti + transformed β-Ti, and transformed β-Ti. The first two phases control the corrosion confrontation of the Ti–Cu alloy (Wang et al., 2019). Niobium is a well-known beta-stabilizing alloying element that enhances the titanium alloy's corrosion resistance (in SBF) and shows excellent biocompatibility (Matsuno et al., 2001; Okazaki et al., 1998). Another study shows that niobium also reduces the castability of the titanium alloy by up to 92.01%. Niobium above 15 % stabilizes the beta phase of titanium, which is best known for its excellent corrosion resistance and lower elastic modulus implant material to manufacture the prosthodontic part (Zhang et al., 2015).

Titanium has weak tribological properties due to its low abrasive wear resistance, which contributes to the letdown of orthopedic joint implants (Hussein et al., 2015). Choubey et al. (2004) show that in steady-state fretting, wear of cpTi shows the highest coefficient of friction compared to other titanium alloys. Abrasive, adhesive, fatigue, fretting, or corrosion wear mechanisms have been identified in orthopedic implants. They depend on various linked parameters such as material composition, surface characteristics, hardness, and corrosion resistance (Revathi et al., 2016). Wear resistance is significant in restorative material because it contributes to robust, long-term occlusion repair. The addition of copper also enhances the wear resistance property of the Ti-alloys. The mechanical properties mainly depend on the microstructure of the alloys; the rich Ti_2Cu phase is responsible for the enhanced wear property (Dong et al., 2018; Ohkubo et al., 2003). The heat treatment process also decides the corrosion resistance of the Ti–Cu alloys (J. Wang et al., 2019). Various research on titanium copper alloy shows that 5% copper is sufficient to improve the mechanical, corrosion, and antibacterial properties of titanium alloys (Liu et al., 2014).

Recently, many studies have been done with binary and ternary titanium alloys for corrosion and wear study (Chapala et al., 2016; Karre et al., 2019; Kent et al., 2013; Salas et al., 2021; Ureña et al., 2019; Wen et al., 2014; Xu et al., 2009; Zhang et al., 2012). In all this research, niobium was considered because of its good corrosion and wear resistance properties. Chapala et al. (2018) reported that the best wear resistance property of titanium exhibited in the α+β phase compared to only the β phase, the fraction of β to α phase decides the wear-resistant property of titanium alloy. Niobium promotes the formation of the beta phase and reduces the elastic modulus; however, the niobium reduces the anti-wear property of the Ti–7Fe alloy (Ehtemam-Haghighi et al., 2016).

Powder metallurgy (PM) has been proven to be an effective alternative technology for producing biomedical implants with controlled porosity, with the added benefit of executing all stages in the solid phase (Mediaswanti et al., 2012). Furthermore, by manipulating processing conditions, powder consolidation can be achieved (Meenashisundaram et al., 2020). PM also enables the creation of beta-Ti alloys at a lower cost, as well as easier processing and the production of small components with complex shapes (Fojt et al., 2013).

Therefore, this study is exclusively focused on studying the effect of microstructure and mechanical properties on the corrosion and tribological behavior of Ti–5Cu-xNb alloys in simulated body fluid solution at room temperature. The detailed study of the processing technique, XRD pattern, the volume fraction of formed phases, microstructure, and mechanical properties of the alloys provided in previous studies (Pandey et al., 2022) and additional corrosion and wear tests of the samples in SBF are thoroughly discussed in this study. The study of the Electrochemical techniques (open circuit potential, electrochemical impedance spectroscopy, and potentiodynamic polarization) was used to investigate the corrosion confrontation behavior of the alloys in the presence of simulated body fluid (pH- 7.4) solution at room temperature. Simultaneously, the tribological behavior of ternary Ti–5Cu-xNb alloy was first studied against zirconia balls at 10 N, 15 N, and 20 N loads in wet conditions. The detailed investigation of wear parameters like the coefficient of friction, worn surface width, maximum lateral depth, wear rate, wear volume, and wear mechanism were successfully discussed in this study. The exposed surface of the alloys following corrosion testing was thoroughly investigated utilizing the SEM and XPS tests. The FESEM image, EDS, analysis, and scanning probe microscopy image of the worn surface area are discussed in detail. This research suggests that alloy design is vital in adjusting the mechanical and wear properties of Ti alloys for biomedical use.

2. Materials and methodology

Ti–5Cu-(x%) Nb (x = 0, 5, 10, and 15 wt%) were sintered by powder metallurgy process. In the desired weight ratio, highly pure titanium, copper, and niobium powder is ball milled for 5 h in the presence of a toluene and argon atmosphere. After ball milling, the milled powder was compacted in a 15 mm diameter tool steel die and sintered at 900 °C for 1 h with a heating rate of 4 °C/minute. Fig. 1 shows the image of the alloy just after sintering (without any treatment). Our earlier research article listed the powder size used for this study and the processing technique (Pandey et al., 2022). The sintering temperature was selected based on previous research to get α, Ti_2Cu, and the transformed phase of α and β-titanium. After sintering, the sample was grounded on SiC paper from 400 to 2500 grit size, then polished with 0.9 μm diamond paste on a velvet cloth. The polished sample was then ultrasonically cleaned in

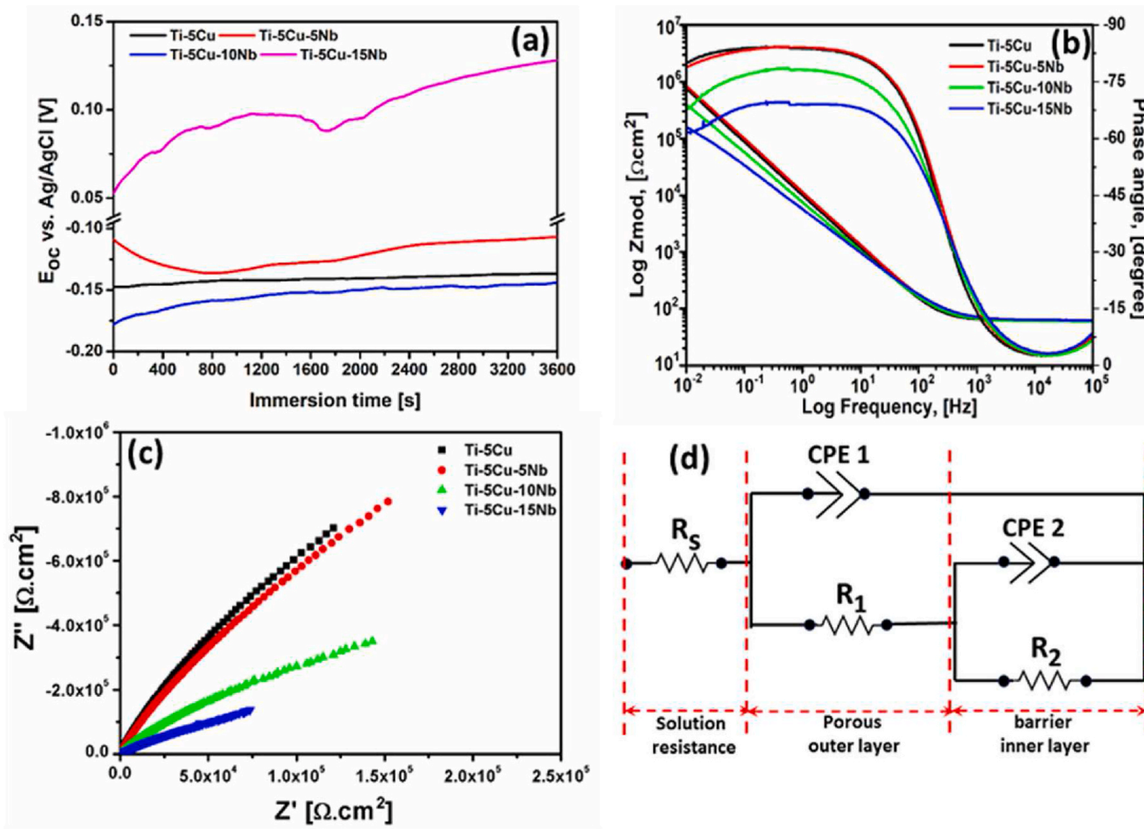

Fig. 2. The open-circuit potential (a), Bode plot (b), Nyquist plot (c), and the proposed equivalent circuit diagram (d) of samples after the OCP and EIS test.

ethanol for 10 min.

2.1. Electrochemical measurements

The Ti–5Cu and Ti–5Cu-(5, 10, 15 %) Nb sintered alloys were evaluated for corrosion performance in SBF (pH = 7.4) at room temperature. The composition of the simulated body fluid is listed in Table 1. The open-circuit potential (OCP), electrochemical impedance spectroscopy (EIS), and potentiodynamic polarization measurement techniques were used to investigate the sintered alloy's corrosion behavior. The electrochemical quantities were carried out in a glass cell at room temperature consisting of a three-electrode cell, which was linked to a potentiostat controlled by a computer (CORRTEST Instruments CS2350 Bi-Potentiostat, China). The uncovered surface (1 cm^2) of the Ti–5Cu and Ti–5Cu-(5, 10, 15 %) Nb samples served as the working electrode in corrosion experiments utilizing the usual three-electrode cell technique [saturated Ag/AgCl as the reference electrode, Platinum sheet as the counter-electrode]. In SBF, the OCP of each alloy was measured continuously for 3600 s. After the OCP measurements, the EIS test was conducted using an A.C. amplitude range of −10 mV to +10 mV and a frequency range of 10^{-2} Hz to 10^{+5} Hz. Using the extrapolation method, the EIS data were explained in Nyquist and Bode-phase plots. After the EIS test, a scan rate of 1 mV per second was used to estimate the potentiodynamic polarization with an initial potential of −1.6 V to +2.1 V from OCP. Tafel analysis based on the polarization plots estimates corrosion parameters such as corrosion potential (E_{corr}) and corrosion current density (i_{corr}), passive current density (i_{pp}), and breakdown potential from the polarization plots. For each group in the experiments, three parallel samples were used. The exposed surface of the sintered alloys just after the corrosion tests were examined by scanning electron microscopy (EVO - Scanning Electron Microscope MA 15/18, Carl Zeiss Microscopy Ltd.) and X-ray photoelectron spectroscopy (K-alpha, Thermo-Fisher Scientific) to analyze the formation and pattern of oxide.

2.2. Wear test

Under wet conditions, the reciprocating wear and friction test of the sintered alloys were tested in an automated Ducom Bio-tribometer (Bengaluru, India). In the tests, the samples acted as the stationary body, whereas the moving body was the counter material. They were performed under lubricated conditions with varying loads to compare different conditions since they have an essential role in the tribological properties of materials. Sintered alloys (φ 15 mm and 4 mm thickness) as a disc and a ZrO_2 ball of 10 mm diameter as counter material were taken for the study. The reciprocating wear track was 5 mm. The normal load of 10, 15, and 20 N was applied to the counter material. The frequency of 2 Hz for 3600 cycles on a 5 mm sliding distance in the presence of SBF was used for all the tests. The length of the wear track was taken as 5 mm (the total stroke length). The wear track's width and lateral depth were measured by a contact profilometer (Taylor and Hobson, England). The wear loss of the worn profile was first measured using a profilometer to calculate the wear loss volume. The average depth values were then calculated using the following formula (Doni et al., 2013):

$$D_{avg} = \frac{A_w}{W} \tag{1}$$

where D_{avg} , A_w, W is the average depth in mm, average wear loss area, and the average width of each worn track, respectively, measured by a profilometer. Finally, wear volume loss was intended with the following formula:

$$\Delta V = \left[\frac{1}{3} * \pi * D_{avg}^2 \left(3R - D_{avg}\right)\right] + A_w * l \tag{2}$$

where Δ V, R, and l are the volume loss (mm^3), the radius of the zirconia ball (mm), and the length of the wear track (5 mm) for each wear track, respectively. The following formula has been used to generate the

Table 2
Impedance constraints of the proposed equivalent circuit attained by fitting the experimental result of EIS.

Sample	R_s (Ωcm^2)	R_1 (Ω cm^2)	CPE_1 (μFcm^{-2})	n_1	$R_2\Omega$ cm^2)	CPE_2 (μFcm^{-2})	n_2	χ^2 (10^{-3})
Ti–5Cu	60.95 (0.3)	1.71×10^{12} (6.5)	18.0 (1.5)	0.93	8.97×10^{6} (1.2)	17.6 (2.3)	0.94	5.4
Ti–5Cu–5Nb	62.27 (0.1)	3.57×10^{12} (10.5)	16.1 (2.3)	0.93	7.45×10^{6} (4.5)	15.4 (3.5)	0.94	6.9
Ti–5Cu–10Nb	59.83 (0.2)	2.10×10^{12} (14.2)	27.4 (2.8)	0.86	1.78×10^{6} (1.8)	26.1 (1.6)	0.88	7.0
Ti–5Cu–15Nb	61.76 (0.4)	4.04×10^{5} (4.5)	36.7 (4.5)	0.80	1.01×10^{6} (2.3)	42.7 (8.5)	0.76	8.0

The percent difference derived from fitting for each component of the analogous circuit is given in parentheses.

volume loss values into wear rate:

$$W_v = \frac{\Delta V}{S} \tag{3}$$

where, W_v denotes the wear rate in mm^3/mm, ΔV is the volume loss in mm^3, and S denotes the overall sliding distance in millimeters.

All experiments were repeated at least three times to achieve repeatability. The wear rates were calculated using three tracks per condition. After the wear test, the sample was ultrasonically cleaned in ethanol for 10 min, then worn surface analysis was done using the 3D surface profilometer (Taylor Hobson, UK), Field emission scanning electron microscopy (FE-SEM, Nova Nano SEM 450) equipped with Energy Dispersive X-ray Spectroscopy (EDS), and scanning probe microscope (SPM, NTEGRA Prima).

3. Results and discussions

3.1. Phase identification, microstructure, and volume fraction

The XRD pattern, microstructure, and volume fraction of formed phases after sintering the samples Ti–5Cu, Ti–5Cu–5Nb, Ti–5Cu–10Nb, and Ti–5Cu–15Nb, showed the formation of α-Ti, an intermetallic compound of Ti and Cu (Ti_2Cu), and transformed β-Ti. The volume fraction of phases identified using the intensity of peaks of XRD data showed that the proportion of the β-Ti phase increases with the addition of niobium in Ti–5Cu. A detailed explanation of formed phases and microstructure is given in our previous study (Pandey et al., 2022).

3.2. Corrosion study

3.2.1. Open-circuit potential

The open-circuit potential relates to the ability of the working electrode with respect to the reference electrode when there is no current supplied, and it reflects the thermodynamic harmony at the metal-solution intersection as a function of time. The response of the open circuit potential concerning the immersion time of Ti–5Cu, Ti–5Cu–5Nb, Ti–5Cu–10Nb, and Ti–5Cu–15Nb in SBF (pH 7.4) is shown in Fig. 2 (a). In the SBF solution, all OCP curves of Ti–Cu and Ti–Cu–Nb sintered alloys shifted higher and became stable, as shown in Fig. 2 (a).

The stable E_{corr} of all four sintered alloys after 1 h was −136 mV, −144 mV, −106 mV, and +128 mV. The initial E_{corr} for the Ti–5Cu–10Nb alloy is nearly −178 mV (Ag/AgCl). Then it progressively increases to honorable potential attainment after 3600 s of immersion to a stable value of approximately −106 mV (Ag/AgCl). Ti–5Cu and Ti–5Cu–5Nb also followed the same variation and reached nobler potential. The OCP curve of Ti–5Cu–15Nb started from 50 mV and ended at 128 mV with significant fluctuation. Besides, the other three samples were shown a lower change in the negative region from start to end, which offers stability in the corrosive media.

3.2.2. EIS measurements

The result obtained from the EIS test of samples is represented through the Bode-phase plot, and the Nyquist plot is shown in Fig. 2 (b) & (c). These diagrams were obtained for the Ti–5Cu and Ti–5Cu-(5–15%) Nb after 3600 s of immersion in SBF.

The bode plot shows that the phase angle approaches 70–85° in the lower to medium frequency range for three alloys except for Ti–5Cu–15Nb. This indicates a highly capacitive behavior and the formation of a highly stable oxide layer on the surface of the alloy in the solution. This is inconsistent with the low current density obtained in the polarization test. In the higher frequency region (10^3–10^5 Hz), the modulus of the impedance of all the alloys becomes constant, associated with a lower phase angle in the bode phase plot indicating a response from solution resistance. Also, from the medium to lower frequency range, the slope of the modulus of Z is nearly −1, which shows that the impedance of the alloy dominates over the resistance of the solution. It could be observed from the bode plot in Fig. 2 (b) that the profiles of the spectra for Ti–5Cu and Ti–5Cu–5Nb almost touched. This indicates that these two alloys' corrosion behavior would not change even in lower pH solutions. However, the profile spectra of Ti–5Cu–15Nb are different and come in the lower phase angle. This indicates the less protective passive layer on the surface of the Ti–5Cu–15Nb.

Any specific attribute associated with the electrochemical performance of the Ti–Cu, and Ti–Cu–Nb cannot be emphasized using these Bode-phase graphs. Any conclusion based on these EIS graphs should be regarded as speculative. These qualitative experimental data allow us to conclude that all Ti–Cu and Ti–Cu–Nb samples analyzed have similar double-layer deposition and a minimum of two times constant, representing Ti–5Cu, and all Ti–Cu–Nb alloys experimentally examined have the same corrosion kinetics and titanium oxide layer establishment. Generally, titanium alloy comprises two protective layers: a porous layer and an inner barrier layer (De Assis et al., 2006; Osório et al., 2010; Venugopalan et al., 2000). Impedance characteristics were estimated using the ZView® tool, utilizing an "equivalent circuit," as shown in Fig. 2 (d), to offer quantitative backing for the observed EIS results. The same circuit diagram is also shown by W.R. Osório et al. (2010) in the EIS test of Ti–Cu in 0.15M NaCl solution and S. L. De Assis(De Assis et al., 2006) in corrosion analysis of Ti6Al4V, Ti–6Al–7Nb, and Ti–13Nb–13Zr in Hank's solution.

According to the model, the oxide layer on Ti–5Cu and Ti–5Cu-(5,10,15%) Nb alloys is believed to have a barrier-like inner layer and a porous outer layer. In this model, R_s, R_1, and R_2 are the resistance offered by the SBF, outer porous layer, and barrier-like inner layer. CPE_1 capacitance of the outer porous layer and CPE_2 capacitance of the inner barrier layer. For the sake of simplicity, a constant-phase element representing a change from the ideal capacitor was utilized instead of the capacitance itself.

The phase element impedance is represented by the formulae $Z_{CPE} = [C(I\omega)^n]^{-1}$ Where C, I, ω is capacitance, current, frequency, and n lies between −1 to 1. The non-uniform distribution of current caused by roughness and surface imperfections is associated with the value of n (Cremasco et al., 2008; Osório et al., 2007). Table 2 shows the solution capacitance, resistance, and n values of the inner-barrier and outer-porous films, which were calculated by fitting the experimental results using the "equivalent circuit" shown in Fig. 2 (d). The value of n near one shows that the behavior of such a layer was similar to that of a perfect capacitor (Lavos-Valereto et al., 2004). The error percentages corresponding to each component of the proposed circuit (numbers provided in Table 2) and the chi-squared (χ^2) values, which stayed on the order of 10^{-3}, were utilized to measure the fitting quality, demonstrating that the data accustomed fit to the recommended predicted circuit.

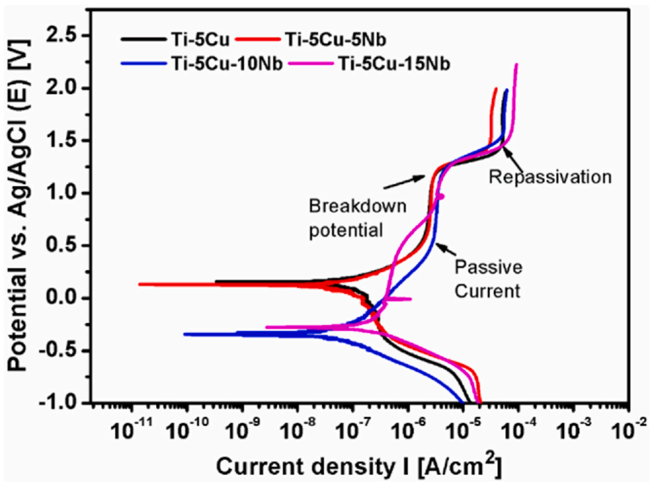

Fig. 3. Potentiodynamic polarization curve of sintered alloys.

Table 3
Corrosion current density, corrosion potential, breakdown potential, passive current, and repassivation current of the sintered alloys.

Parameters	Ti–5Cu	Ti–5Cu–5Nb	Ti–5Cu–10Nb	Ti–5Cu–15Nb
Corrosion Current density i_{corr} [nA cm^{-2}]	40.12 (±3.12)	31.07 (±4.17)	21.44(±2.15)	106.37 (±11.32)
Corrosion Potential E_{corr} [mV]	143 (±10)	11.7(±2)	−339(±14)	−277(±17)
Breakdown Potential [mV]	1155 (±20)	1155(±20)	1146(±25)	1274(±30)
Passive Current [μA cm^{-2}]	2.07 (±0.58)	2.25(±.89)	2.83(1.01)	3.02(±1.14)
Repassivation Current [μA cm^{-2}]	51.7 (±8.1)	30.4(±4.15)	51.5(±14.2)	71.5(±21.65)

The resistance offered by the outer porous layer of Ti–5Cu–15Nb is 4.04×10^5 Ω cm^2 which is the lowest in comparison to another three alloys. It indicates the Ti–5Cu–15Nb alloy is less stable in the corrosive medium. On the other hand, the resistance offered by the outer porous layer (R_1) by Ti–5Cu–5Nb is the highest, indicating that the outer porous layer is more resistant to SBF than other alloys. When comparing the capacitances CPE_1 (outer-porous layer) of the Ti–5Cu, Ti–5Cu–5Nb, Ti–5Cu–10Nb, and Ti–5Cu–15Nb using the proposed equivalent circuit, similar tendencies are detected: average values of about 18, 16.1, 27.4, and 36.7 μFcm^{-2} obtained, respectively. However, for all Ti–5Cu, Ti–5Cu–5Nb, Ti–5Cu–10Nb, and Ti–5Cu–15Nb, the CPE_2 (inner-barrier layer) has lesser measured values than the CPE_1. Low capacitances are related to an increase in the thickness of the protective film (Cremasco et al., 2008; De Assis et al., 2006; Osório et al., 2010) and a drop in the dielectric constant of the oxide film (due to changes in the electrolytic solution volume/oxide film ratio) (Cremasco et al., 2008; Gudi et al., 2002; M. Aziz-Kerrzo, K.G. Conroy, A.M. Fenelon, S.T. Farell, 2001). ((De Assis et al., 2006)) showed that the inner-barrier coating delivers corrosion protection, and (Osório et al., 2010) indicated that both the inner and outer protective layer is responsible for corrosion fortification. In the present study, the lower value of R_2 compared to R_1 for Ti–5Cu, Ti–5Cu–5Nb, and Ti–5Cu–10Nb alloys indicated that the outer porous layer is predominantly responsible for corrosion protection.

Fig. 2 (c) shows the Nyquist plot of the experimental data obtained by the EIS test of Ti–5Cu, Ti–5Cu–5Nb, Ti–5Cu–10Nb, and Ti–5Cu–15Nb sintered alloys in SBF. By comparing the ($Z_{imaginary}$ vs. Z_{real} ratio) of the Ti–5Cu and Ti–5Cu–5Nb samples, the slope of the semi-arc is nearly identical, as shown in Fig. 2 (c). With increasing niobium percentage, the slope also decreases. Based on the discussion and results shown in Table 2, the Ti–5Cu, Ti–5Cu–5Nb, and Ti–5Cu–10Nb show better corrosion resistance than Ti–5Cu–15Nb in simulated body fluid solution.

The potentiodynamic anodic polarization performance of the Ti–5Cu, Ti–5Cu–5Nb, Ti–5Cu–10Nb, and Ti–5Cu–15Nb sintered alloys in SBF is evaluated, and the experimental and computed impedance values are approved.

3.2.3. Potentiodynamic polarization behavior

The potentiodynamic polarization results of Ti–5Cu, Ti–5Cu–5Nb, Ti–5Cu–10Nb, and Ti–5Cu–15Nb alloys in SBF solutions, are shown in Fig. 3. Polarization parameters, including corrosion current density (i_{corr}), corrosion potential (E_{corr}), passive current density (i_{pp}), breakdown potential, and re-passivation current density, were attained using standard procedures from the potentiodynamic polarization graphs, as listed in Table 3. The anodic and cathodic slopes of the Tafel plot were considered for calculating current density and corrosion potential. The intersection point of the slope of the anodic and cathodic curves decides the E_{corr} and i_{corr} values. From the OCP value of the Tafel plot, (+50 mV) was added to the anodic side, and a (−50 mV) value was added to the cathodic side. Then the slopes from these points were taken into consideration. The primary polarization current (i_{pp}), breakdown potential, and re-passivation current were obtained directly from the anodic branch of the Tafel plot.

The corrosion potential (E_{corr}) obtained from the polarization slightly differs from open circuit potential measurements. This is expected, as the polarization measurements started at a cathodic potential (−1.6 V to OCP) so that the E_{corr} (polarization) increases for Ti–5Cu and Ti–5Cu–5Nb and decreases for Ti–5Cu–10Nb and Ti–5Cu–15Nb. This deviation in the potential reduces the passive film at the surface due to highly reducing initial potentials. It can be observed from the Tafel plot that i_{corr} reduces with increasing niobium up to 10%, and sudden increases for Ti–5Cu–15Nb are also shown in Table 3. The slope of the anodic branch for Ti–5Cu and Ti–5Cu–5Nb is approximately the same, but Ti–5Cu–10Nb and Ti–5Cu–15Nb are not the same as the other two. The faster growth of the potential from E_{corr} for the Ti–5Cu–10Nb indicates that the passive layer is slightly replaced by the less protective film, which becomes stable at 2.83×10^{-6} (A/cm^2) current density. This point is called passive current density(i_{pp}). The passive current density for all the sintered alloys is nearly (2–3 μA-cm^{-2}), the lowest for Ti–5Cu and the maximum for Ti–5Cu–15Nb.

The highest value of the i_{pp} of the Ti–5Cu–15Nb indicates a defect in the oxide film and the formation of a more irregular porous protective layer. At around 1.17×10^{-7} (A/cm^2), the potential for Ti–5Cu–15Nb increases faster and becomes stable at −3.7 mV. The current density oscillation shows that the passive film is breaking down, similar to the pitting formation and re-passivation situation. However, the breakdown potential of the sintered alloys is nearly the same. All the sintered alloys show the re-passivation at around (1500–1550 mV to Ag/AgCl). After the first breakdown of the initial protective layer, the new layer formed suddenly, and it became stable till the remaining applied potential. The corrosion rate directly relates to the corrosion current density; as shown in Table 3, the current density of the Ti–5Cu decreases with increasing niobium percentage up to 10%. The Ti–5Cu–15Nb has a higher percentage of niobium; thus, β-Ti stabilizes more than α+Ti_2Cu; thus, the corrosion potential decreases rapidly compared to the other three alloys. In earlier research, J. Wang et al. (J. Wang et al., 2019) also reported that transformed β-Ti causes a negative influence on the corrosion vulnerability of Ti–5Cu alloys. Although the Ti_2Cu phase improves the corrosion confrontation, it can correspondingly form a galvanic cell with α or β-phase, which further increases the corrosion rate of the alloy in SBF(Liu et al., 2017). The volume fraction of Ti_2Cu and β-phase is highest in Ti–5Cu–15Nb, compared to the other three alloys, which show the lowest corrosion potential. In the present study, the i_{corr} value of Ti–5Cu–10Nb (21.44 nA cm^{-2}) lies between the i_{corr} value of Ti13Nb13Zr, and Ti6Al4V (De Assis et al., 2006) when tested in

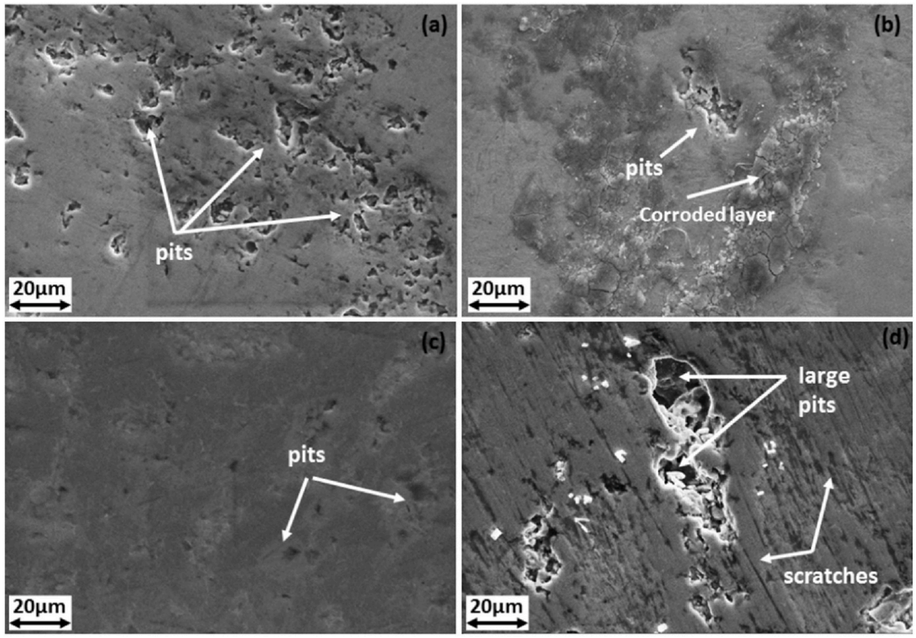

Fig. 4. SEM image of sample (a) Ti–5Cu, (b) Ti–5Cu–5Nb, (c) Ti–5Cu–10Nb, and (d) Ti–5Cu–15Nb after potentiodynamic polarization test.

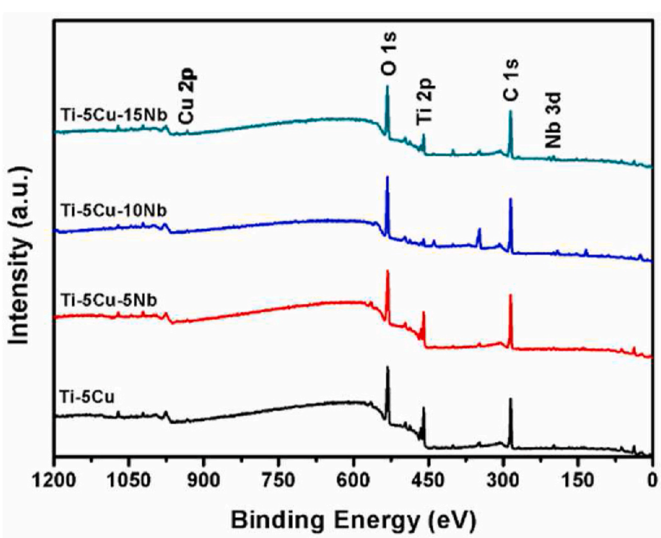

Fig. 5. XPS spectra of the sintered alloy after the potentiodynamic polarization test.

naturally aerated Hank's solution. Based on the above results, the present research resolved that incorporating niobium enhances the corrosion potential of Ti–5Cu alloys in SBF compared to i_{corr} value in recent research on Ti–Cu alloys (Gui et al., 2016; Tao et al., 2020; Zhang et al., 2016, 2013).

3.3. Surface investigation

Fig. 4(a–d) shows the typical SEM microstructure of the Ti–5Cu, Ti–5Cu–5Nb, Ti–5Cu–10Nb, and Ti–5Cu–15Nb sintered alloys after the potentiodynamic polarization test in SBF. The surface morphology of Ti–5Cu in Fig. 4 (a) indicates that some localized corrosion occurs along with many corrosion micro-pit. In Fig. 4 (b), the corroded surface of Ti–5Cu–5Nb revealed the formation of the oxides layer, which protected the alloys during anodic corrosion. This layer reduces the localized corrosion and micro-pits compared to Fig. 4 (a). The SEM image of Ti–5Cu–10Nb in Fig. 4 (c) has less oxide formation than Ti–5Cu and Ti–5Cu–5Nb. The corrosion current density (i_{corr}) of Ti–5Cu–15Nb is maximum, as shown in Table 3, and the SEM image, as shown in Fig. 4 (d), proved the same. The entire surface affected by the corrosion and very rough surface, along with macro-pits, is shown in the image. Ti–5Cu–15Nb corroded more badly compared with the other three alloys in SBF. The α+Ti_2Cu and α+transformed β-Ti phases are mainly responsible for protecting against chemical attacks(J. Wang et al., 2019).

In the previous study, the corroded SEM image of Ti–Ag in artificial saliva reported by B. B. Zhang et al. (2009) showed nearly the same as in the present study. The surface of the corroded Ti–Nb alloy is mainly composed of TiO_2 and Nb_2O_5 (Bai et al., 2011) when tested in various electrolytes composed of artificial saliva and modified artificial saliva solution. In the present study, the same compound formed on alloys' surfaces, further proved by the XPS study.

Figs. 5 and 6 show the XPS spectra of corroded surfaces of all the alloys after the potentiodynamic corrosion test to know the phases and oxide compounds formed after corrosion. The XPS spectra revealed the main composition of the surface layer of Ti–5Cu, Ti–5Cu–5Nb, Ti–5Cu–10Nb, and Ti–5Cu–15Nb alloys after tests in SBF were TiO_2, CuO, and Nb_2O_5. The chemical bonds of O1s for Ti–5Cu, Ti–5Cu–5Nb, Ti–5Cu–10Nb, and Ti–5Cu–15Nb were determined as shown in Fig. 6 (a): oxygen was present at the surface of Ti–5Cu, Ti–5Cu–5Nb, Ti–5Cu–10Nb, and Ti–5Cu–15Nb with binding energies of $E_b = 530.47$ eV, 530.47 eV 530.27 eV, and 530.87 eV, respectively. The binding energy of TiO_2 was also shown in Fig. 6 (b) as 458.87 eV, 458.87 eV, 459.07 eV, and 458.87 eV, respectively. The binding energy of Nb_2O_5 for Ti–5Cu–5Nb, Ti–5Cu–10Nb, and Ti–5Cu–15Nb are 207.38 eV, 207.87 eV, and 207.38 eV are respectively. Both copper and niobium are known for the enhancement of corrosion resistance.

Copper formed CuO compound with oxygen with higher bind energy of 932.98 eV, 932.68 eV, 932.98 eV, and 932.57 eV, respectively.

The open-circuit potential measurements, electrochemical impedance spectroscopy studies, and polarization tests all agreed with the SEM and XPS studies.

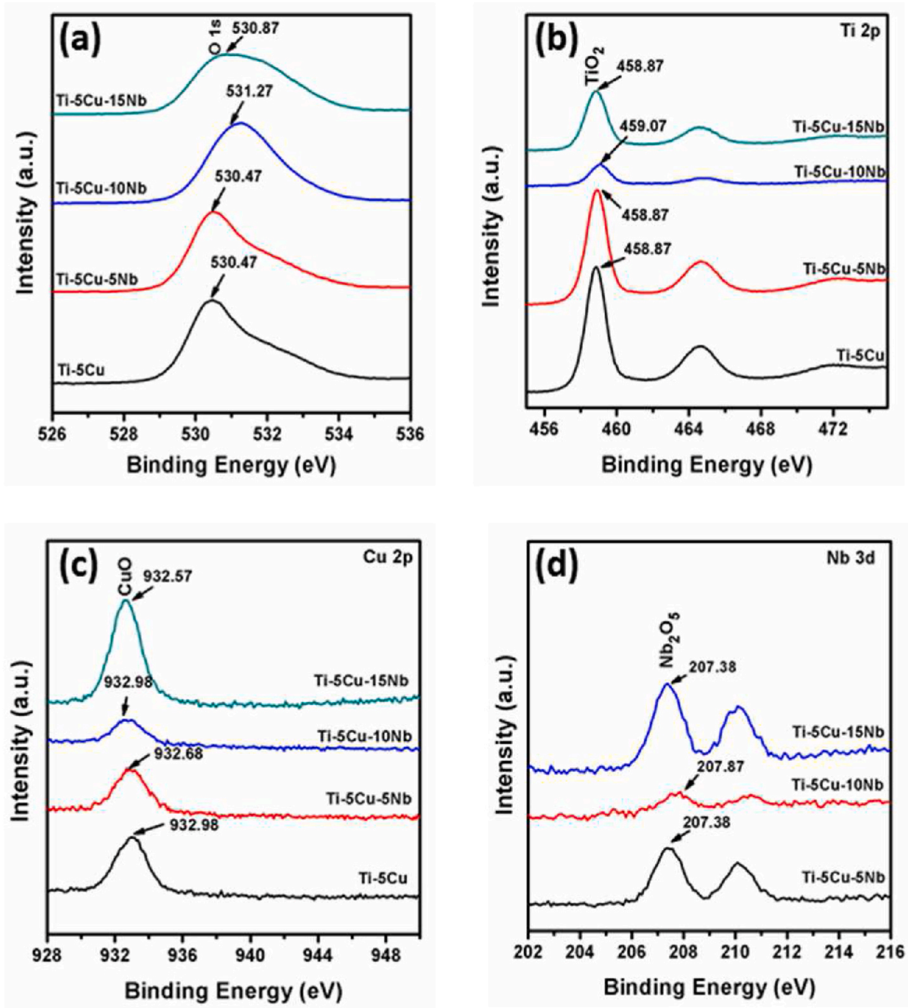

Fig. 6. XPS spectra of (a) Oxygen, (b) Titanium, (c) Copper, and (d) Niobium.

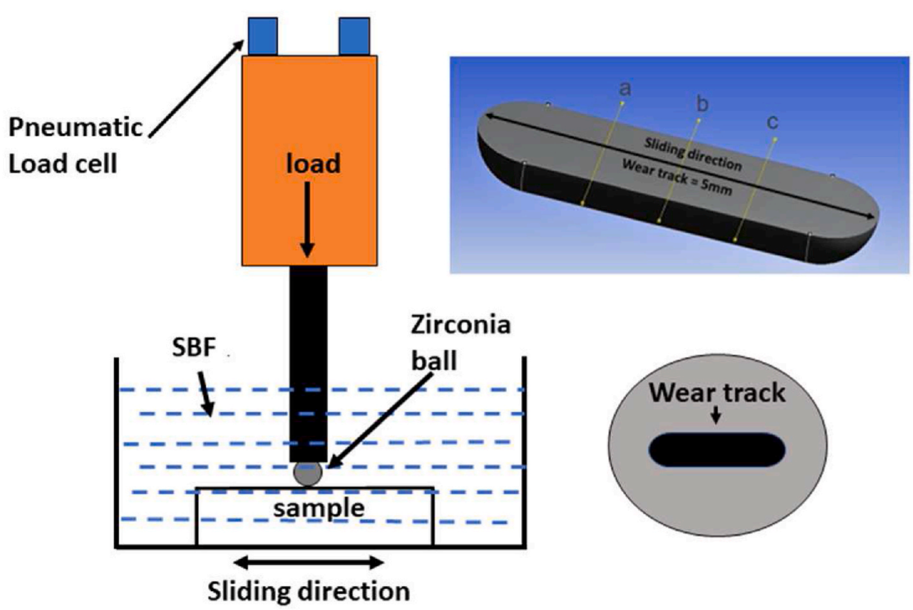

Fig. 7. Schematic diagram of wear testing and wear track of sample in the presence of SBF.

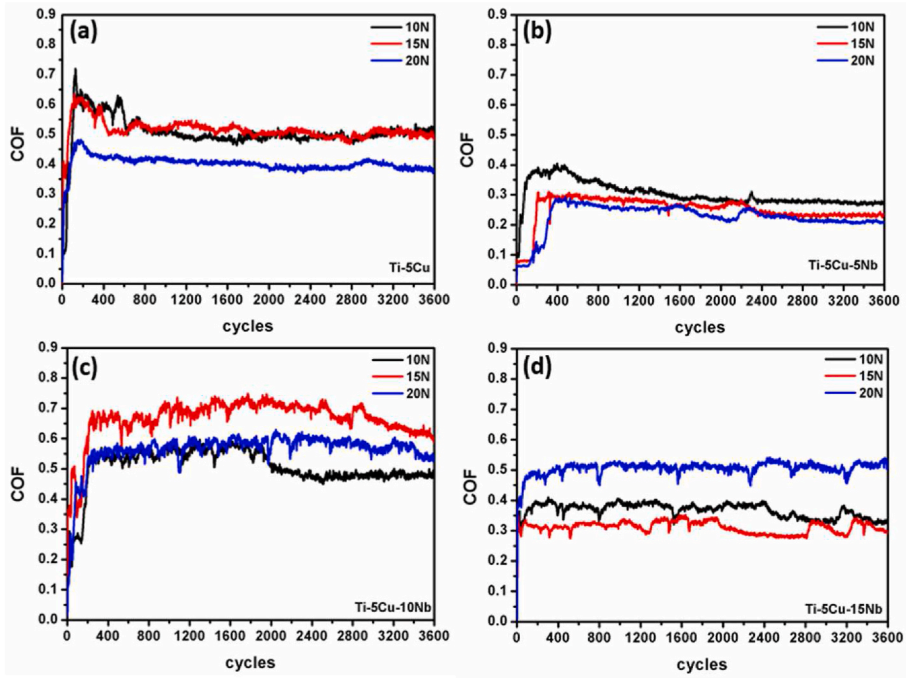

Fig. 8. Coefficient of friction vs. running cycles graph of (a) Ti–5Cu, (b) Ti–5Cu–5Nb, (c) Ti–5Cu–10Nb, and (d) Ti–5Cu–15Nb at 10 N, 15 N, and 20 N loads, respectively.

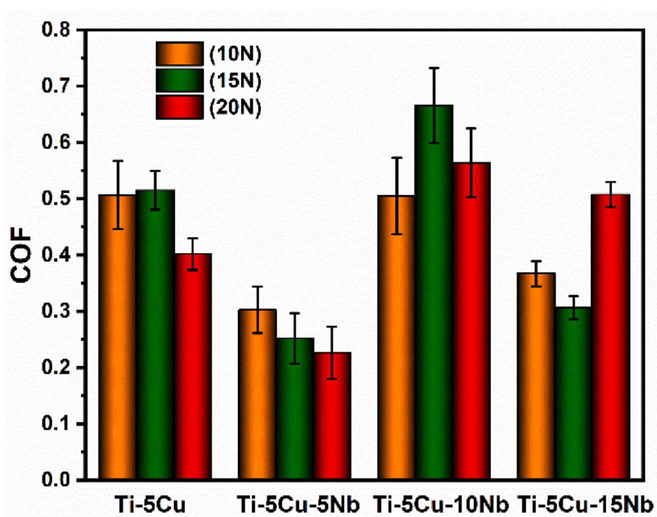

Fig. 9. Average friction coefficient of sintered alloys running after 3600 cycles at 10 N, 15 N, and 20 N load, respectively.

Table 4
Parameter and results obtained after the wear test of the samples in SBF.

Sample	Load (N)	wear scar width (μm)	max. Depth (μm)	volumetric wear $\times 10^{-3}$ (mm^3)	Wear rate $\times 10^{-8}$ (mm^3/mm)
Ti–5Cu	10	523	3.24	3.85	5.36
	15	642	4.01	6.20	8.61
	20	681	5.14	9.28	12.88
Ti–5Cu–5Nb	10	579	8.27	15.49	21.51
	15	777	11.01	25.83	35.87
	20	825	12.20	34.11	47.38
Ti–5Cu–10Nb	10	959	17.30	44.58	61.92
	15	1181	21.20	82.98	115.25
	20	1227	24.40	101.81	141.41
Ti–5Cu–15Nb	10	911	14.80	42.98	59.70
	15	894	16.90	44.64	62.00
	20	1126	26.60	104.38	144.97

3.4. *Wear and frictional behavior of alloys*

3.4.1. *Coefficient of friction value*

Fig. 7 depicts the schematic diagram of the wear study and the worn profile of samples in wet conditions against zirconia ball.

Fig. 8 shows the coefficient of friction vs. running cycle graph of Ti–5Cu-(0,5,10,15%Nb) at 10 N, 15 N, and 20 N load, respectively. In Fig. 8 (a), the cof value of Ti–5Cu at 10 N load attained a maximum value of 0.71 shortly after the experiment started and became steady after 1000 cycles. A similar variation in cof value was obtained at 15 N load; also, the maximum cof reached slightly lower than 10 N load. However, at 20 N load, the maximum cof attained a value of 0.48 at the initial stage, and it remained steady after completing 150 cycles. Accordingly, the maximum and minimum cof values were attained at 10 N and 20 N loading, respectively. The average cof values at 10 N, 15 N, and 20 N loads were 0.506 ± 0.061, 0.515 ± 0.034, and 0.402 ± 0.028 recorded for the 3600 cycles. Ti–5Cu–5Nb followed the same tendency of maximum and minimum cof values for 10 N and 20 N loading, as shown in Fig. 8 (b). The average cof value 0.302 ±.0041, 0.252 ± 0.044, and 0.227 ± 0.046 were obtained accordingly at 10 N, 15 N, and 20 N loads. The cof vs. running cycle plot of Ti–5Cu–10Nb, as shown in Fig. 8 (c), reveals that the alloy obtained a maximum cof value at a 15 N load with an average cof value of 0.665 ± 0.067, while the minimum cof value at 10 N load with an average of 0.505 ± 0.068. The average cof value increases by 31.68% at 15 N load compare to 10 N load. The cof value of Ti–5Cu–15Nb with respect to the running cycle shows a relatively constant value throughout the whole running period, as shown in Fig. 8 (d). The average cof 0.367 ± 0.022, 0.311 ± 0.012, and 0.506 ± 0.023 were gained at 10 N, 15 N, and 20 N load, respectively, as depicted in Fig. 9. The cof value against sliding distance for Ti–5Cu–10Nb, and Ti–5Cu–15Nb shows an unstable or fluctuating profile at all three loading conditions. Based on the average cof value, Ti–5Cu–5Nb is less prone to wear than the other three samples, while Ti–5Cu–15Nb is more

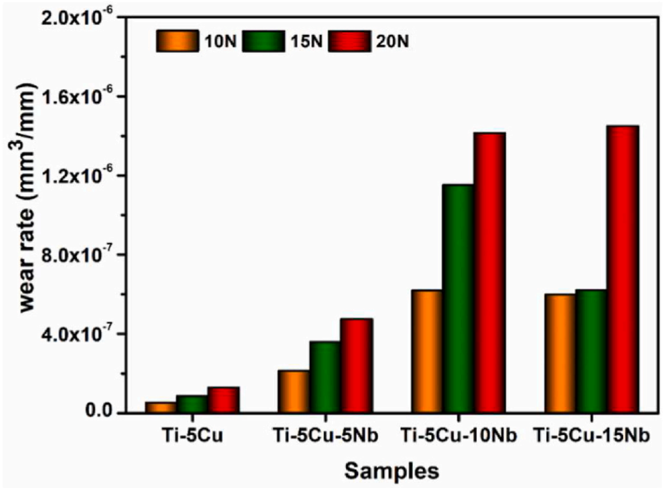

Fig. 10. Wear rate of all four samples running after 3600 cycles against zirconia ball in SBF.

favorable to wear against the zirconia counterpart in SBF.

The friction coefficient depends on the magnitude of the load, surface condition, and the relative hardness of mating parts (Uthayakumar et al., 2013). In Fig. 8 (a) and (b), increasing the load reduces the average coefficient of friction; at the early stage, the alloy structure is slightly pressed. During the second stage, some particles slowly disengage at the two points of interaction, and more and more particles detach with increasing load (Xu et al., 2013). The loose particles or wear debris acts as a lubricant between mating zirconia ball and samples. However, this trend is not the same for the average cof value of Ti–5Cu–10Nb, and Ti–5Cu–15Nb, Fig. 8 (c) & (d). The SEM image of Ti–5Cu–10Nb, 15N, and 20N load (Fig. 13) show the worn surface area content of the grooves, delamination, and adhesion; this might be the possible reason for the maximum average cof value at a higher load (Doni et al., 2013). (Xu et al., 2013) also reported that 5% Nb showed a lower coefficient of friction than 10%, 15%, and 20% Nb in Ti–15Mo alloy; the same average cof value was also observed in present investigation.

3.4.2. Worn surface width and lateral depth

The wear scar profile measured by profilometer of samples Ti–5Cu, Ti–5Cu–5Nb, Ti–5Cu–10Nb, and Ti–5Cu–20Nb is demonstrated in Figs. S1 and S2 (in supplementary file), in which the wear area of the 2D profile and maximum lateral depth are quantified and calculated. Compared to the wear track profiles at 15 N and 20 N loading conditions, the wear track profile of Ti–5Cu at 10 N load is not considerably smooth. Furthermore, the worn surface profile of Ti–5Cu–5Nb at 10 N and 15 N loads is not as uniform as at 20 N loads. It is due to the accumulation of wear particles on the worn surface. The maximum depth and lateral width of the wear scar are reported in Table 4.

On the other hand, the smooth surface has the lowest coefficient of friction, but the wear volume loss is more significant than the non-smooth surface. The same result of volumetric wear loss of smooth surface can be seen here, reported in Table 4. At 20 N load, the worn surface profile became wider and deep for Ti–5Cu–5Nb, resulting in the highest wear loss and worst wear resistance (Fig. S1 (f)). As shown in Fig. S2, the worn surface profile of Ti–5Cu–10Nb and Ti–5Cu–15Nb against the zirconia ball differs from Fig. S1. Although the width of the worn surface increases with increasing load for Ti–5Cu–10Nb compared to Ti–5Cu and Ti–5Cu–5Nb, this trend does not apply with Ti–5Cu–15Nb. As illustrated in Fig. S3 (a), the wear track width of

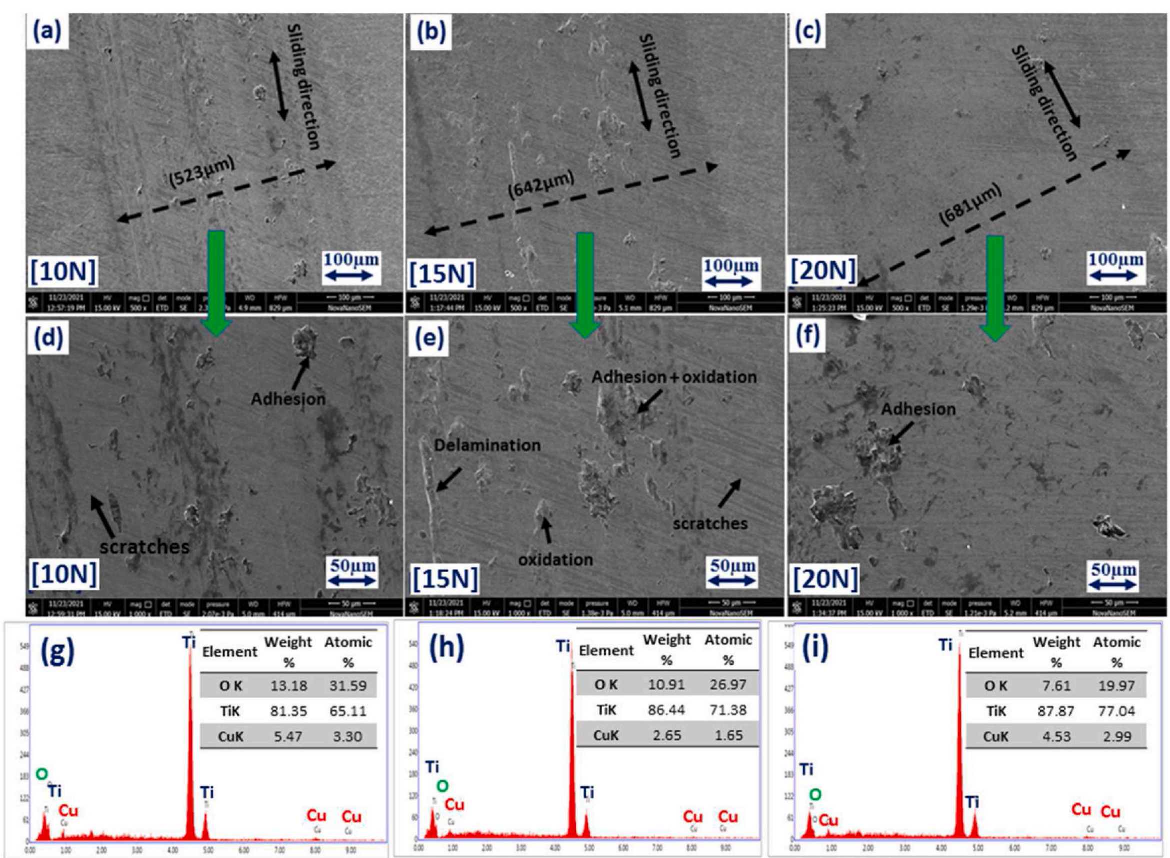

Fig. 11. The SEM image and EDS analysis of the worn surface of Ti–5Cu at 10 N (a,d,g), 15 N (b,e,h), and 20 N (c,f,i) load after 3600 cycles.

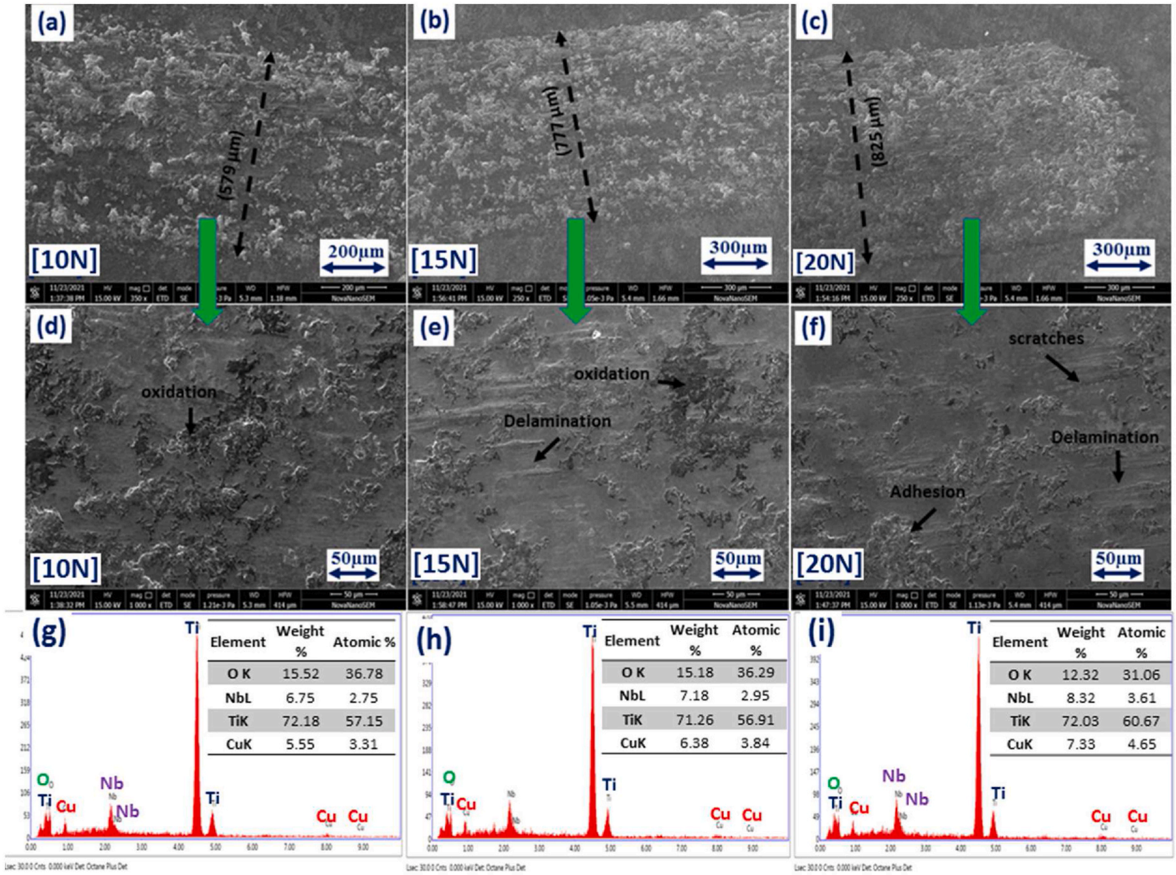

Fig. 12. The SEM micrograph and EDS analysis of the worn surface of Ti–5Cu–5Nb at 10 N (a,d,g), 15 N (b,e,h), and 20 N (c,f,i) load after 3600 cycles.

Ti–5Cu–15Nb is less than Ti–5Cu–10Nb for 10 N, 15 N, and 20 N loads. The wear track width of sample Ti–5Cu–10Nb was recorded 1181 μm and 1227 μm for 15 N and 20 N loads, respectively, which was the widest of all the samples. Additionally, the maximum lateral depth of the worn profile was obtained for Ti–5Cu–15Nb at 20 N load.

Fig. S3 (b) depicts the maximum lateral depth of worn surfaces measured by the profilometer for all four samples under three loading conditions. Ti–5Cu–10Nb recorded maximum depths of 17.3 μm and 21.2 μm under 10 N and 15 N loads, respectively. Also, at 20 N loads, the wear depth increases as the niobium percentage to Ti–5Cu increases, reaching a maximum of 26.6 μm for Ti–5Cu–15Nb. As illustrated in Fig. 8, the average cof value of Ti–5Cu–10Nb at 10 N, 15 N, and 20 N loads are maximum compared to the other three samples. The same trend we can observe in Fig. S3 (a) and (b). Higher cof values for Ti–5Cu–10Nb at 10 N and 15 N loads exacerbated the lateral maximum depth and width simultaneously to wear track, but at 20 N load, the counter material mainly increases width, not depth. Based on this finding, we can conclude that increasing the load or stress applied to the Ti–5Cu–15Nb will reduce the lateral penetration and widen the wear track. At three loading conditions, Ti–5Cu had the smallest breadth and lateral depth of wear track of all the samples, indicating that it is more wear-resistant.

The depth and width of the wear track largely depend upon the material's hardness, density, microstructure, and elastic modulus (Fellah et al., 2013). The wear depth of the material depends upon the hardness of the counter material (Iijima et al., 2003). As stated in our previous study (Pandey et al., 2022), the Vicker micro-hardness value of Ti–5Cu is the highest compared to the other three samples. Also, the maximum depth of the worn surface increases with increasing loads and niobium percentage in Ti–5Cu. Compared to Ti–5Cu, the maximum depth and waviness are highest for Ti–5Cu–5Nb. However, the cof value is the lowest for Ti–5Cu–5Nb. The wear debris between the mating part acts as a lubricant and lowers the cof compared to Ti–5Cu.

3.4.3. *Wear volume and wear rate*

Wear volume and wear rate are evaluated using equations (2) and (3) based on the result finding of wear track width and average lateral depth. The wear rate varies with load and sample compositions, as shown in Fig. 10. Table 4 shows that at 10 N load, Ti–5Cu–10Nb has a maximum wear rate of 6.19239×10^{-7} (mm^3/mm), while Ti–5Cu has a minimum wear rate of 5.35916×10^{-8} (mm^3/mm). The wear rate increased by approximately 10.5 times by adding 10 wt% niobium to Ti–5Cu at 10 N load against zirconia counter material. Furthermore, Ti–5Cu–15Nb has shown 3.5% lower wear rate than Ti–5Cu–10Nb under the same loading conditions. The wear rate at the 15 N loading condition follows the same pattern for all samples. Moreover, at 20 N load, the wear rate continuously increased with increasing niobium to Ti–5Cu and reached the maximum value of 1.44976×10^{-6} (mm^3/mm) in SBF against the zirconia ball. Based on these wear rate data, Ti–5Cu has outstanding anti-wear properties against zirconia balls, whereas niobium inclusion in Ti–5Cu has a negative impact on strength in a reciprocating motion.

The wear rate mainly depends on the surface material's mechanical properties (hardness, density, elastic modulus, load applied, and Hertzian contact pressure) and the hardness of the counterpart material. The wear rate mainly depends on the H/E (hardness/elastic modulus) ratio (Ehtemam-Haghighi et al., 2016). The hardness and elastic modulus of the alloys were calculated and given in our previous study; the H/E ratio of the alloy decreases with increasing niobium percentage. This might be the main reason behind the increasing wear rate of the alloy against the zirconia ball. The SEM image of the microstructure of the alloys and volume fraction of phases indicates the formation of the beta phase with

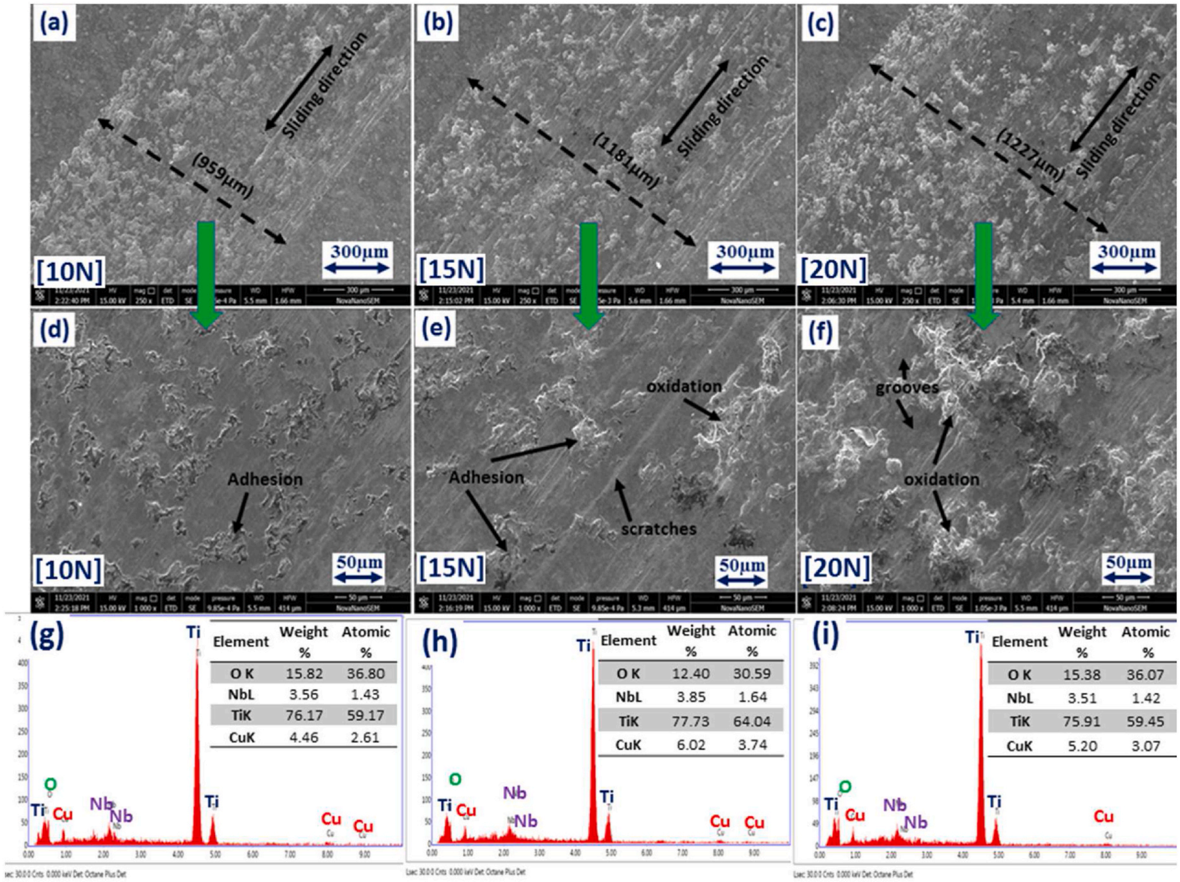

Fig. 13. The SEM micrograph and EDS analysis of the worn surface of Ti–5Cu–10Nb at 10 N (a,d,g), 15 N (b,e,h), and 20 N (c,f,i) load after 3600 cycles.

increasing niobium percentage. The higher beta phase is less stable in mechanical abrasion, and the breakdown of passive layers continuously occurs. Ehtemam-Haghighi S (Ehtemam-Haghighi et al., 2016) showed in their research that the maximum beta phase is responsible for the increased wear rate of the alloys. Although the wear rate of the samples used in this study is increasing with niobium addition, this is relatively less than in other earlier studies. The maximum loading condition and lesser density of the samples with niobium addition might be the main reason behind the higher wear rate.

3.4.4. Worn surface characterization

Fig. 11 shows the scanning electron microscopy (SEM) image and energy dispersive X-ray spectroscopy (EDS) analysis of the worn surfaces of Ti–5Cu at three loading conditions. The average cof value of Ti–5Cu alloy at 15 N load is maximum compared to 10 N and 20 N load (Fig. 9), and the scratches in SEM images of the worn surfaces reveal the same. The possible reason for maximum scratches is the early breakdown of the passive oxide layer, which resulted in direct contact between the zirconia ball and the alloy surface. The worn surface image of Ti–5Cu at 20 N load has minimum oxide and the adhesive layer, resulting in the minimum average cof value during the whole cycle compared to other loading conditions. The width of the worn surface follows the loading condition and increases with increasing load, as shown in Fig. 11. The maximum width of the wear track was observed at 20 N load, which is 30% more than the width at 10 N load. Moreover, surface delamination was also observed at the 15 N loading of Ti–5Cu. The EDS analysis of the selected area shows the presence of O, Ti, and Cu.

Fig. 12 shows the SEM image of the worn surface of Ti–5Cu–5Nb at different loading conditions, and the EDS report of the selected area is shown in Fig. 12 (d, e, and f). As shown in Fig. 8 (b), the cof value decreases with increasing load; the same pattern can also observe in the SEM image of worn surfaces (Fig. 12). Fig. 12 (a) has maximum whitish and black debris of oxides as compared to Fig. 12 (b) and (c), which causes the maximum cof value. With increasing load, the cof value decreases accordingly while the wear track width increases. The EDS report of the selected region of Fig. 12 (d, e, and f) shows the presence of O, Ti, Cu, and Nb.

Fig. 13 shows the SEM image and EDS analysis of worn surfaces of Ti–5Cu–10Nb against the zirconia ball in SBF. All the samples exhibit typical indications of adhesion with a few disparities. The correlation between the presence of niobium in EDS, the SEM image, and the cof value can be observed in Fig. 13. The maximum cof value was obtained for Ti–5Cu–10Nb at 15 N load, and the corresponding SEM image in Fig. 13 (e) shows that oxide layer depletion and surface-to-surface contact of zirconia ball and sample. The lowest niobium presence in the EDS might be the reason for the maximum cof value. Both copper and niobium percent in EDS reports are significantly low, indicating the formation of copper oxide, niobium oxide, and titanium oxide caused by abrasion, adhesion, and excessive temperature between the contact surfaces.

Fig. 14 shows the three wear tracks of Ti–5Cu–15Nb at 10 N, 15 N, and 20 N loads. The lowest friction coefficient was obtained for 15 N load and the highest for 20 N. The worn surface SEM image comprises adhesion, scratches, oxidative layer, and grooves. The width of the wear track was observed to be lower than Ti–5Cu–10Nb, while depth increases comparatively. Also, the grooves in Fig. 14 (f) at 20 N loads confirm the higher cof value and maximum lateral depth compared to the cof value and lateral depth at 10 N and 15 N loading conditions. The EDS reports of elements for the 15 N load of Fig. 14 (e) are shown in Fig. 14 (h). The niobium weight percent compare to other loading is the highest and might be the reason for the lowest friction coefficient.

The lowest cof value was recorded for Ti–5Cu–5Nb at 20 N load,

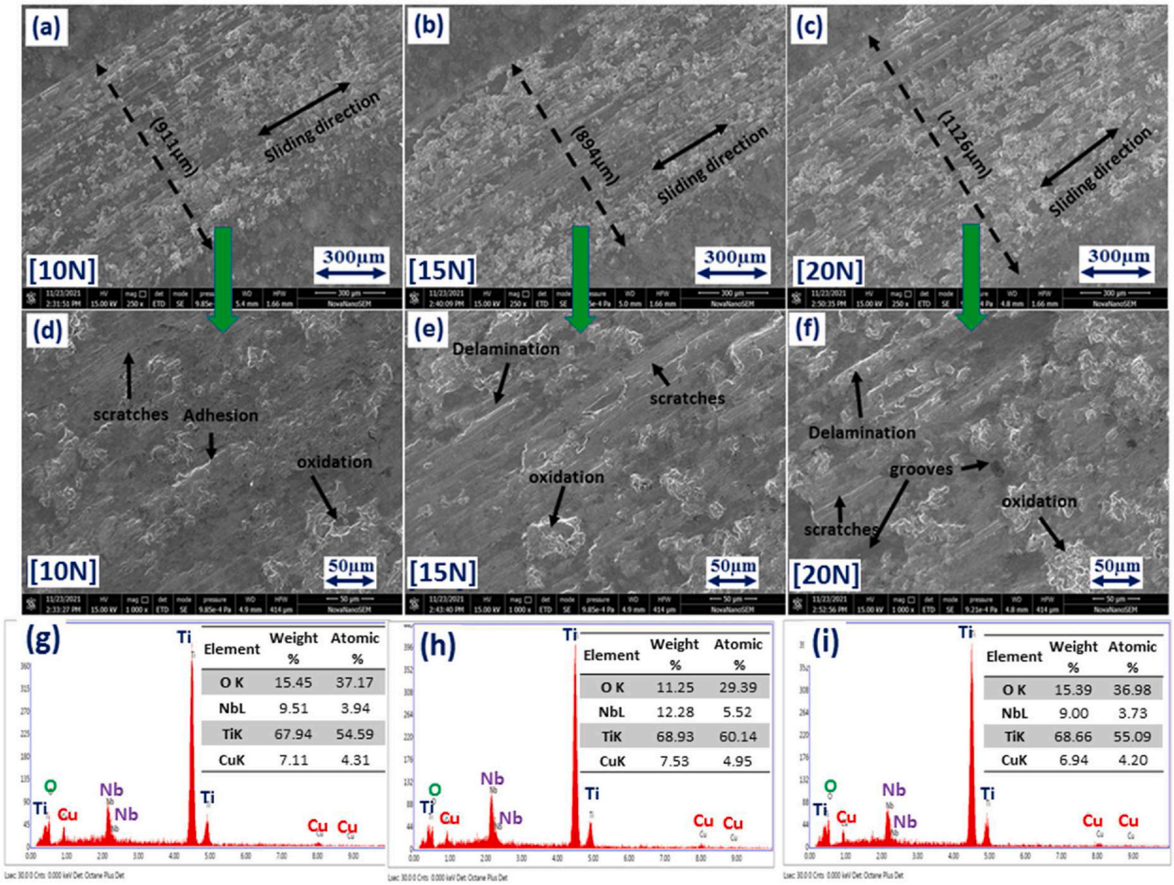

Fig. 14. The SEM micrograph and EDS analysis of the worn surface of Ti–5Cu–15Nb at 10 N (a,d,g), 15 N (b,e,h), and 20 N (c,f,i) load after 3600 cycles.

Table 5
The summary of surface roughness of worn surface for different loading.

Samples		Line roughness		Surface roughness	
		R_a, nm	R_q, nm	S_a, nm	S_q, nm
Ti–5Cu	10 N	19.68	27.18	37.93	56.13
	15 N	27.34	48.17	46.40	70.97
	20 N	24.07	39.12	28.86	48.89
Ti–5Cu–15Nb	10 N	166.47	235.35	381.72	493.75
	15 N	154.55	210.36	342.8	459.68
	20 N	190.35	256.4	376.12	579.25

while the highest was for Ti–5Cu-10 Nb at 15 N load against zirconia ball in SBF. Furthermore, the EDS analysis at the selected point on the worn area was conducted to investigate the reason for the differences in cof value. Figs. S4 and S5 show the EDS analysis at the selected point on worn surface SEM images of Ti–5Cu–5Nb, and Ti–5Cu–10Nb, respectively, at that particular loading conditions. Fig. S4 (a) shows the SEM image of the worn surface under 20 N load and four different EDS points with varying appearances. The dark grey phase at spot 1 shows the presence of bare titanium. At the same time, wt.% of other elements like O, Nb, and Cu is lower than 10%, indicating the dominant adhesion wear mechanism and corresponding to Ti, Nb, and Cu oxide(Ureña et al., 2018). The EDS analysis of Spot 2 shows the copper-rich phase, whereas spot 3 shows the oxide of copper and niobium, as the oxygen percentage is higher than spot 2. According to the EDS result, spot 4 is light grey and contains titanium oxide.

In Fig. S5, spot 2 (black phase) shows a less percentage of niobium and copper which further depicts the presence of oxide of both Nb and Cu, while the plane surface at spot 1 represents the copper-rich phase, same as spot 2 of Fig. S4. Furthermore, spots 3 and 4 (white color) have a higher percentage of oxygen, indicating the production of oxide due to oxidation, adhesion, and abrasion between the counterpart and sample. The worn surface shows that the grooves and scratches mark parallel to the wear track, a typical example of an abrasive mark-cutting mechanism. The abrasion between asperities of sample Ti–5Cu–10Nb and zirconia ball greatly enhances the cof value (Akbarpour and Moniri Javadhesari, 2017).

3.4.5. Scanning probe microscope analysis

The maximum and minimum losses in wear volume were observed in Ti–5Cu, and Ti–5Cu–15Nb, respectively, after the wear test. The SPM analysis was used to investigate the effect of surface roughness on volume loss. The linear and surface roughness parameters of the worn surface obtained after SPM analysis by Gwyddion software are shown in Table 5. The surface topography of the worn surfaces at different loads of Ti–5Cu and Ti–5Cu–15Nb is shown in Figs. 15 and 16, respectively. On the worn surface, a 60*60 μm^2 area was taken for study. For Ti–5Cu, the maximum friction coefficient was observed at 10 N load, and the presence of numerous peaks and valleys, as shown in Fig. 15 (d) compared to Fig. 15 (e and f), proved the same. However, the maximum height of peaks on the worn surface of Fig. 15 (d) is the lowest (0.63 μm) compared to the maximum height of the worn surface of Ti–5Cu at 15 N (1.15 μm) and 20 N (1.2 μm) load. The surface topography of the worn surface of sample Ti–5Cu, at 15 N load shows the smooth plane in some regions, as shown in Fig. 15 (e). The wear volume and wear rate increase with increasing load; also, at 20 N load, the surface topography of the worn surface shows the maximum volume loss. The wear mechanism in the 20 N load shows adhesion, abrasion, and oxidation.

The surface topography of the worn surface of Ti–5Cu–15Nb is shown in Fig. 16. The surface roughness of the sample at all three

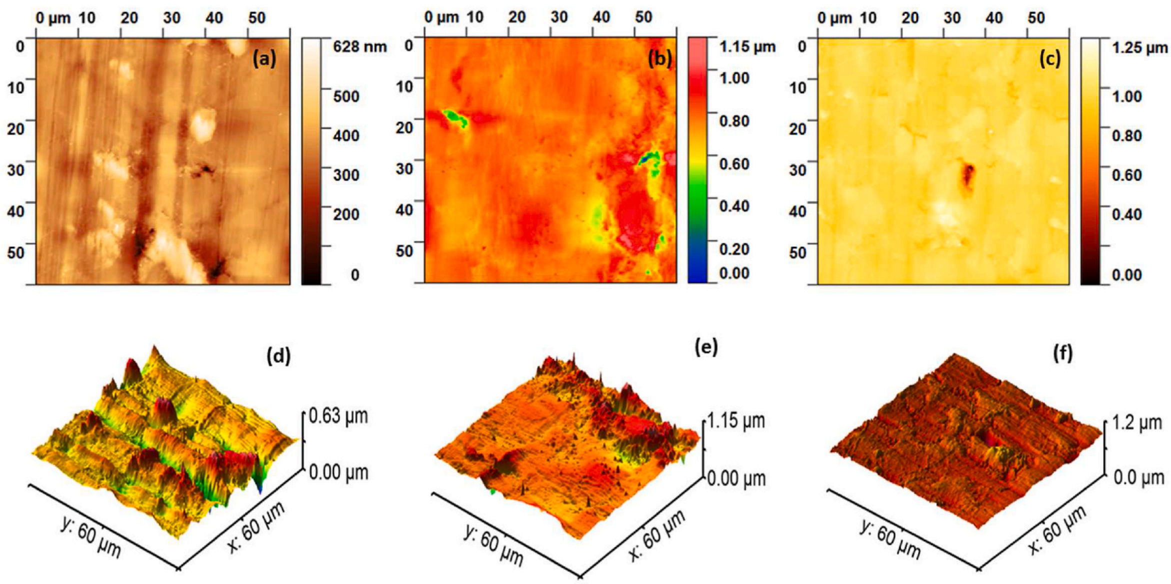

Fig. 15. Worn surface topography of Ti–5Cu at (a) 10 N, (b) 15 N, and (c) 20 N load, and images (d), (e), (f) are 3D surface topography, respectively.

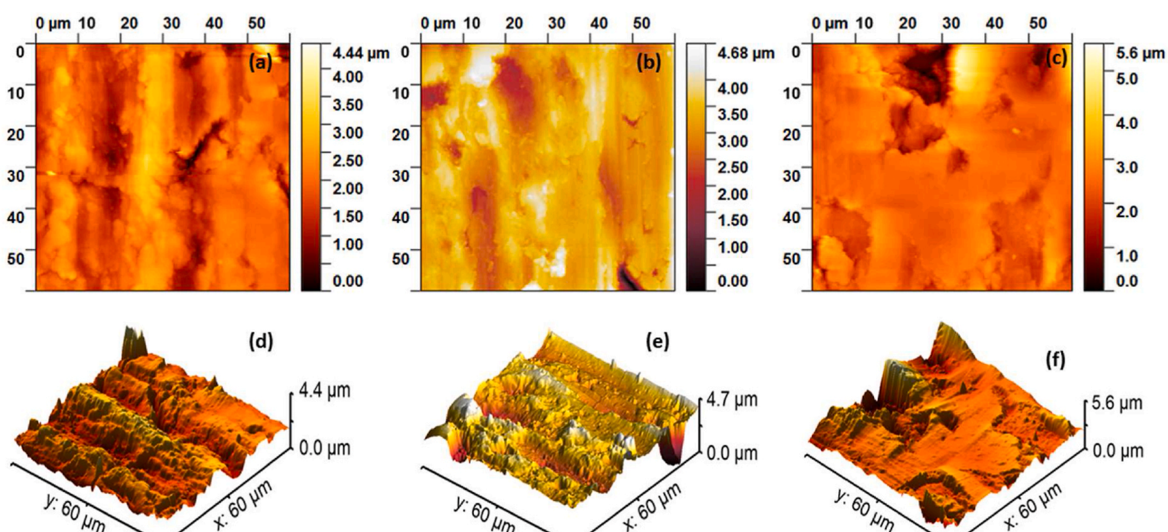

Fig. 16. Worn surface topography of Ti–5Cu–15Nb at (a) 10 N, (b) 15 N, and (c) 20 N load, and images (d), (e), (f) are 3D surface topography, respectively.

loading conditions is solely different according to the result of wear loss volume. At the 10 N loading condition, the maximum height of the peaks from the valley is the lowest compared to 15 N and 20 N loading conditions, as shown in Fig. 16 (a). The wear profile of the substrate at 10 N load is parallel to the sliding direction, while the 20 N load is slightly different. This results in a higher friction coefficient at 10 N load than in 15 N loading conditions. However, the wear profile of the substrate at 20 N load is different, and maximum roughness caused the higher cof value. The maximum loss in wear volume was obtained at 20 N loading condition; the peak to valley height for this is maximum compared to others. It can be seen from Fig. 16 (f) that the wear profiles of the substrate have deep grooves, sharp edges, delamination, and accumulation of particles; this confirms the material lost by abrasion, adhesion, and oxidation(Lu et al., 2020).

4. Conclusions

In the present studies, the outcome of niobium addition to Ti–5Cu alloys, keeping the copper equivalence close to 5 wt%, has been examined with respect to the corrosion and wear resistance of the alloys in SBF (pH = 7.4) at room temperature. The observation from combined conventional electrochemical analysis (namely, OCP, EIS, and anodic polarization), scanning electron microscopy, and the XPS spectra study of post corrosion test, as well as the tribological performance of samples in SBF against zirconia counterpart, have led to the following conclusions:

1. After immersion in SBF, all of the examined Ti–5Cu–5Nb, Ti–5Cu–10Nb, and Ti–5Cu–15Nb alloys passivated spontaneously, and passive films have capacitive behavior similar to Ti–5Cu.
2. The EIS measurements showed a double protective layer on the surface of alloys immersed in the SBF. The outer porous layer is stronger than the inner barrier layer except for Ti–5Cu–15Nb.
3. Adding niobium to Ti–5Cu alloys significantly improves the corrosion resistance of alloys in the SBF.
4. Potentiodynamic polarization evidence shows a significant drop-in corrosion rate and the passive current densities with the addition of Nb up to 10% in Ti–5Cu.

5. The SEM and XPS analyses confirmed the electrochemical results, revealing that the passive layer is composed of TiO_2, Nb_2O_5, and CuO. And Ti–5Cu–10Nb is the most corrosion-resistant alloy in SBF.
6. The wear rate of the alloys increases with increasing niobium percentage and maximum for Ti–5Cu–15Nb at 20 N load. However, for the same sample, the wear rate at 10 N and 15 N load is lower than Ti–5Cu–10Nb. Also, the volumetric loss of samples was comparatively much lower than cPTi and Ti6Al4V at the same loading conditions.
7. The worn surface analysis showed that the wear mechanism comprises adhesion, oxidation, abrasion, and delamination.
8. The corrosion and wear study of the samples showed that Ti–5Cu–10Nb is more corrosion-resistant and less wear-resistant in simulated body fluid to the zirconia counterpart.
9. Excellent corrosion and wear-resistant properties are required to manipulate the phases and mechanical properties of the alloys properly. Also, the present alloys can be considered to replace the cPTi and Ti6Al4V for biomedical applications.

CRediT authorship contribution statement

Anurag Kumar Pandey: Writing – original draft, Methodology, Investigation, Formal analysis, Data curation, Conceptualization. **R.K. Gautam:** Writing – review & editing, Project administration, Funding acquisition. **C.K. Behera:** Writing – review & editing.

Declaration of competing interest

The authors declare that they have no known competing financial interests or personal relationships that could have appeared to influence the work reported in this paper.

Data availability

No data was used for the research described in the article.

Acknowledgments

The Department of Science and Technology of the Government of India provided financial support, which the author would like to recognize (SERB sanction order number: EEQ/2018/000949). The instrument analysis and testing center, Central Instrument Facility, Indian Institute of Technology (BHU), Varanasi, India, is especially appreciative.

Appendix A. Supplementary data

Supplementary data to this article can be found online at https://doi.org/10.1016/j.jmbbm.2022.105533.

References

Akbarpour, M.R., Moniri Javadhesari, S., 2017. Wear performance of novel nanostructured Ti-Cu intermetallic alloy as a potential material for biomedical applications. J. Alloys Compd. 699, 882–886. https://doi.org/10.1016/j.jallcom.2017.01.020.

Aziz-Kerrzo, M., Conroy, K.G., Fenelon, A.M., Farell, S.T., C.B.B, 2001. Electrochemical studies on the stability and corrosion resistance of titanium-based implant materials. Biomaterials 22, 1531–1539.

Bai, Y.J., Wang, Y.B., Cheng, Y., Deng, F., Zheng, Y.F., Wei, S.C., 2011. Comparative study on the corrosion behavior of Ti-Nb and TMA alloys for dental application in various artificial solutions. Mater. Sci. Eng. C 31, 702–711. https://doi.org/10.1016/j.msec.2010.12.010.

Barth, E., Myrvik, Q.M., Wagner, W., Gristina, A.G., 1989. In vitro and in vivo comparative colonization of Staphylococcus aureus and Staphylococcus epidermidis on orthopaedic implant materials. Biomaterials 10, 325–328. https://doi.org/10.1016/0142-9612(89)90073-2.

Cao, B., Zheng, Y., Xi, T., Zhang, C., Song, W., Burugapalli, K., Yang, H., Ma, Y., 2012. Concentration-dependent cytotoxicity of copper ions on mouse fibroblasts in vitro: effects of copper ion release from TCu380A vs TCu220C intra-uterine devices. Biomed. Microdevices 14, 709–720. https://doi.org/10.1007/s10544-012-9651-x.

Chapala, P., Acharyya, S.G., Shariff, S.M., Naik, G., 2016. Novel Ti-Nb alloys with improved wear resistance for biomedical implant application. In: Proceedings of the Annual International Conference of the IEEE Engineering in Medicine and Biology Society. EMBS, pp. 4208–4211. https://doi.org/10.1109/EMBC.2016.7591655.

Chapala, P., Acharyya, S.G., Shariff, S.M., Bhattacharjee, A., 2018. Studying the effect of composition on the in vitro wear behavior and elastic modulus of titanium-niobium-based alloys for biomedical implants. Biomed. Phys. Eng. Express 4. https://doi.org/10.1088/2057-1976/aa9f78.

Choubey, A., Basu, B., Balasubramaniam, R., 2004. Tribological behaviour of Ti-based alloys in simulated body fluid solution at fretting contacts. Mater. Sci. Eng., A 379, 234–239. https://doi.org/10.1016/j.msea.2004.02.027.

Cremasco, A., Osório, W.R., Freire, C.M.A., Garcia, A., Caram, R., 2008. Electrochemical corrosion behavior of a Ti-35Nb alloy for medical prostheses. Electrochim. Acta 53, 4867–4874. https://doi.org/10.1016/j.electacta.2008.02.011.

De Assis, S.L., Wolynec, S., Costa, I., 2006. Corrosion characterization of titanium alloys by electrochemical techniques. Electrochim. Acta 51, 1815–1819. https://doi.org/10.1016/j.electacta.2005.02.121.

Dong, R., Zhu, W., Zhao, C., Zhang, Y., Ren, F., 2018. Microstructure, mechanical properties, and sliding wear behavior of spark plasma sintered Ti-Cu alloys. Metall. Mater. Trans. A Phys. Metall. Mater. Sci. 49, 6147–6160. https://doi.org/10.1007/s11661-018-4953-0.

Doni, Z., Alves, A.C., Toptan, F., Gomes, J.R., Ramalho, A., Buciumeanu, M., Palaghian, L., Silva, F.S., 2013. Dry sliding and tribocorrosion behaviour of hot pressed CoCrMo biomedical alloy as compared with the cast CoCrMo and Ti6Al4V alloys. Mater. Des. 52, 47–57. https://doi.org/10.1016/j.matdes.2013.05.032.

Ehtemam-Haghighi, S., Prashanth, K.G., Attar, H., Chaubey, A.K., Cao, G.H., Zhang, L.C., 2016. Evaluation of mechanical and wear properties of Ti-xNb-7Fe alloys designed for biomedical applications. Mater. Des. 111, 592–599. https://doi.org/10.1016/j.matdes.2016.09.029.

Elias, C.N., Fernandes, D.J., Resende, C.R.S., Roestel, J., 2015. Mechanical properties, surface morphology and stability of a modified commercially pure high strength titanium alloy for dental implants. Dent. Mater. 31, e1–e13. https://doi.org/10.1016/j.dental.2014.10.002.

Fellah, M., Assala, O., Labaïz, M., Dekhil, L., Iost, A., 2013. Friction and wear behavior of Ti-6Al-7Nb biomaterial alloy. J. Biomaterials Nanobiotechnol. 374–384. https://doi.org/10.4236/jbnb.2013.44047, 04.

Fojt, J., Joska, L., Málek, J., 2013. Corrosion behaviour of porous Ti-39Nb alloy for biomedical applications. Corrosion Sci. 71, 78–83. https://doi.org/10.1016/j.corsci.2013.03.007.

Gao, C., Yao, M., Shuai, C., Peng, S., Deng, Y., 2019. Nano-SiC reinforced Zn biocomposites prepared via laser melting: microstructure, mechanical properties and biodegradability. J. Mater. Sci. Technol. 35, 2608–2617. https://doi.org/10.1016/j.jmst.2019.06.010.

Geetha, M., Singh, A.K., Asokamani, R., Gogia, A.K., 2009. Ti based biomaterials, the ultimate choice for orthopaedic implants - a review. Prog. Mater. Sci. 54, 397–425. https://doi.org/10.1016/j.pmatsci.2008.06.004.

Gudi, S., Radoševi, J., Kliški, M., 2002. Study of passivation of Al and Al-Sn alloys in borate buffer solutions using electrochemical impedance spectroscopy. Electrochim. Acta 47, 3009–3016. https://doi.org/10.1016/S0013-4686(02)00246-3.

Gui, V., Amigó, V., Mu, A.I., 2016. Microstructural, Electrochemical and Tribo-Electrochemical Characterisation of Titanium-Copper Biomedical Alloys, vol. 109, pp. 115–125.

Heidenau, F., Mittelmeier, W., Detsch, R., Haenle, M., Stenzel, F., Ziegler, G., Gollwitzer, H., 2005. A novel antibacterial titania coating: metal ion toxicity and in vitro surface colonization. J. Mater. Sci. Mater. Med. 16, 883–888. https://doi.org/10.1007/s10856-005-4422-3.

Hussein, M.A., Mohammed, A.S., Al-Aqeeli, N., 2015. Wear characteristics of metallic biomaterials: a review. Materials 8, 2749–2768. https://doi.org/10.3390/ma8052749.

Iijima, D., Yoneyama, T., Doi, H., Hamanaka, H., Kurosaki, N., 2003. Wear properties of Ti and Ti-6Al-7Nb castings for dental prostheses. Biomaterials 24, 1519–1524. https://doi.org/10.1016/S0142-9612(02)00533-1.

Karre, R., Kodli, B.K., Rajendran, A., Nivedhitha, J., Pattanayak, D.K., Ameyama, K., Dey, S.R., 2019. Comparative study on Ti-Nb binary alloys fabricated through spark plasma sintering and conventional P/M routes for biomedical application. Mater. Sci. Eng. C 94, 619–627. https://doi.org/10.1016/j.msec.2018.10.006.

Kent, D., Wang, G., Dargusch, M., 2013. Effects of phase stability and processing on the mechanical properties of Ti-Nb based β Ti alloys. J. Mech. Behav. Biomed. Mater. 28, 15–25. https://doi.org/10.1016/j.jmbbm.2013.07.007.

Khan, M.S., ur Rehman, S., Ali, M.A., Sultan, B., Sultan, S., 2008. Infection in orthopedic implant surgery, its risk factors and outcome. J. Ayub Med. Coll. Abbottabad 20, 23–25.

Lavos-Valereto, I.C., Wolynec, S., Ramires, I., Guastaldi, A.C., Costa, I., 2004. Electrochemical impedance spectroscopy characterization of passive film formed on implant Ti-6AI-7Nb alloy in Hank's solution. J. Mater. Sci. Mater. Med. 15, 55–59. https://doi.org/10.1023/B:JMSM.0000010097.86245.74.

Liu, H.Y., Wang, X.J., Wang, L.P., Lei, F.Y., Wang, X.F., Ai, H.J., 2008. Effect of fluoride-ion implantation on the biocompatibility of titanium for dental applications. Appl. Surf. Sci. 254, 6305–6312. https://doi.org/10.1016/j.apsusc.2008.03.075.

Liu, J., Li, F., Liu, C., Wang, H., Ren, B., Yang, K., Zhang, E., 2014. Effect of Cu content on the antibacterial activity of titanium-copper sintered alloys. Mater. Sci. Eng. C. https://doi.org/10.1016/j.msec.2013.11.028.

Liu, L., He, M., Xu, X., Zhao, C., Gan, Y., Lin, Junjie, Luo, J., Lin, Jinxin, 2017. Preliminary study on the corrosion resistance, antibacterial activity and cytotoxicity of selective-laser-melted Ti6Al4V-xCu alloys. Mater. Sci. Eng. C 72, 631–640. https://doi.org/10.1016/j.msec.2016.11.126.

Lu, X., Zhang, D., Xu, W., Yu, A., Zhang, Jiazhen, Tamaddon, M., Zhang, Jianliang, Qu, X., Liu, C., Su, B., 2020. The effect of Cu content on corrosion, wear and tribocorrosion resistance of Ti-Mo-Cu alloy for load-bearing bone implants. Corrosion Sci. 177, 1–8. https://doi.org/10.1016/j.corsci.2020.109007.

Matsuno, H., Yokoyama, A., Watari, F., Uo, M., Kawasaki, T., 2001. Biocompatibility and osteogenesis of refractory metal implants, titanium, hafnium, niobium, tantalum and rhenium. Biomaterials 22, 1253–1262. https://doi.org/10.1016/S0142-9612(00)00275-1.

Mediaswanti, K., Wen, C., Evanova, E., Berndt, C., Wang, J., 2012. Powder metallurgy : a promising route for bone implants fabrication. High Temp. Process. Symp. 2012 42–44.

Meenashisundaram, G.K., Wang, N., Maskomani, S., Lu, S., Anantharajan, S.K., Dheen, S. T., Nai, S.M.L., Fuh, J.Y.H., Wei, J., 2020. Fabrication of Ti + Mg composites by three-dimensional printing of porous Ti and subsequent pressureless infiltration of biodegradable Mg. Mater. Sci. Eng. C 108, 110478. https://doi.org/10.1016/j.msec.2019.110478.

Mitsuo, N., 1998. Mechanical properties of biomedical titanium alloys. Mater. Sci. Eng., A 243, 231–236.

Ohkubo, C., Shimura, I., Aoki, T., Hanatani, S., Hosoi, T., Hattori, M., Oda, Y., Okabe, T., 2003. Wear resistance of experimental Ti-Cu alloys. Biomaterials 24, 3377–3381. https://doi.org/10.1016/S0142-9612(03)00157-1.

Okazaki, Y., Rao, S., Tateishi, T., Ito, Y., 1998. Cytocompatibility of various metal and development of new titanium alloys for medical implants. Marterials Sci. Eng. A 243, 250–256.

Osório, W.R., Spinelli, J.E., Ferreira, I.L., Garcia, A., 2007. The roles of macrosegregation and of dendritic array spacings on the electrochemical behavior of an Al-4.5 wt.% Cu alloy. Electrochim. Acta 52, 3265–3273. https://doi.org/10.1016/j.electacta.2006.10.004.

Osório, W.R., Cremasco, A., Andrade, P.N., Garcia, A., Caram, R., 2010. Electrochemical behavior of centrifuged cast and heat treated Ti-Cu alloys for medical applications. Electrochim. Acta 55, 759–770. https://doi.org/10.1016/j.electacta.2009.09.016.

Pandey, A.K., Gautam, R.K., Behera, C.K., 2022. Microstructure, mechanical strength, chemical resistance, and antibacterial behavior of Ti-5Cu-x%Nb biomedical alloy. Biomed. Mater. 17, 045022 https://doi.org/10.1088/1748-605X/ac7763.

Ren, Ling, zheng, ma, li, mei, 2014. Antibacterial properties of Ti-6Al-4V-xCu alloys _ elsevier enhanced Reader.pdf. J. Mater. Sci. Technol. 30, 699–705.

Revathi, A., Magesh, S., Balla, V.K., Das, M., Manivasagam, G., 2016. Current advances in enhancement of wear and corrosion resistance of titanium alloys – a review. Mater. Technol. 31, 696–704. https://doi.org/10.1080/10667857.2016.1212780.

Salas, L., Chávez, J., Jimenez, O., Flores-Jimenez, M., Alvarado-Hernandez, F., Olmos, L., Pérez-Alvarez, J., Flores, M., 2021. Tribocorrosion and corrosion behavior of quaternary Ti-24Nb-xZr-ySn alloys in SBF. Mater. Lett. 283 https://doi.org/10.1016/j.matlet.2020.128903.

Samuni, A., Chevion, M., Czapski, G., 1984. Roles of copper and O2 in the radiation-induced inactivation of T7 bacteriophage. Radiat. Res. 99, 562. https://doi.org/10.2307/3576330.

Sohail, M.R., Henrikson, C.A., Braid-Forbes, M.J., Forbes, K.F., Lerner, D.J., 2011. Mortality and cost associated with cardiovascular implantable electronic device infections. Arch. Intern. Med. 171, 1821–1828. https://doi.org/10.1001/archinternmed.2011.441.

Sterritt, R.M., Lester, J.N., 1980. Interactions of heavy metals with minerals. Sci. Total Environ. 14, 5–17.

Szaraniec, B., Goryczka, T., 2017. Structure and properties of Ti-Ag alloys produced by powder metallurgy. J. Alloys Compd. 709, 464–472. https://doi.org/10.1016/j.jallcom.2017.03.155.

Taddei, E.B., Henriques, V.A.R., Silva, C.R.M., Cairo, C.A.A., 2004. Production of new titanium alloy for orthopedic implants. Mater. Sci. Eng. C 24, 683–687. https://doi.org/10.1016/j.msec.2004.08.011.

Taira, M., Moser, J.B., Greener, E.H., 1989. Studies of Ti alloys for dental castings. Dent. Mater. 5, 45–50. https://doi.org/10.1016/0109-5641(89)90093-6.

Tao, S.C., Xu, J.L., Yuan, L., Luo, J.M., Zheng, Y.F., 2020. Microstructure, mechanical properties and antibacterial properties of the microwave sintered porous Ti–3Cu alloys. J. Alloys Compd. 812, 1–9. https://doi.org/10.1016/j.jallcom.2019.152142.

Thurman, R.B., Gerba, C.P., 1989. The molecular mechanisms of copper and silver ion disinfection of bacteria and viruses. Crit. Rev. Environ. Control 18, 295–315. https://doi.org/10.1080/10643388909388351.

Ureña, J., Tsipas, S., Pinto, A.M., Toptan, F., Gordo, E., Jiménez-Morales, A., 2018. Corrosion and tribocorrosion behaviour of β-type Ti-Nb and Ti-Mo surfaces designed by diffusion treatments for biomedical applications. Corrosion Sci. 140, 51–60. https://doi.org/10.1016/j.corsci.2018.06.024.

Ureña, J., Tabares, E., Tsipas, S., Jiménez-Morales, A., Gordo, E., 2019. Dry sliding wear behaviour of β-type Ti-Nb and Ti-Mo surfaces designed by diffusion treatments for biomedical applications. J. Mech. Behav. Biomed. Mater. 91, 335–344. https://doi.org/10.1016/j.jmbbm.2018.12.029.

Uthayakumar, M., Aravindan, S., Rajkumar, K., 2013. Wear performance of Al-SiC-B4C hybrid composites under dry sliding conditions. Mater. Des. 47, 456–464. https://doi.org/10.1016/j.matdes.2012.11.059.

Venugopalan, R., Weimer, J.J., George, M.A., Lucas, L.C., 2000. The effect of nitrogen diffusion hardening on the surface chemistry and scratch resistance of Ti-6Al-4V alloy. Biomaterials 21, 1669–1677. https://doi.org/10.1016/S0142-9612(00)00049-1.

Wang, J., Zhang, S., Sun, Z., Wang, H., Ren, L., Yang, K., 2019. Optimization of mechanical property, antibacterial property and corrosion resistance of Ti-Cu alloy for dental implant. J. Mater. Sci. Technol. 35, 2336–2344. https://doi.org/10.1016/j.jmst.2019.03.044.

Wen, M., Wen, C., Hodgson, P., Li, Y., 2014. Fabrication of Ti-Nb-Ag alloy via powder metallurgy for biomedical applications. Mater. Des. 56, 629–634. https://doi.org/10.1016/j.matdes.2013.11.066.

Xu, L.J., Xiao, S.L., Tian, J., Chen, Y.Y., Huang, Y.D., 2009. Microstructure and dry wear properties of Ti-Nb alloys for dental prostheses. Trans. Nonferrous Met. Soc. China (English Ed. 19, 2–7. https://doi.org/10.1016/S1003-6326(10)60124-0.

Xu, L.J., Xiao, S.L., Tian, J., Chen, Y.Y., 2013. Microstructure, mechanical properties and dry wear resistance of β-type Ti-15Mo-xNb alloys for biomedical applications. Trans. Nonferrous Met. Soc. China (English Ed. 23, 692–698. https://doi.org/10.1016/S1003-6326(13)62518-2.

Zhang, B.B., Zheng, Y.F., Liu, Y., 2009. Effect of Ag on the corrosion behavior of Ti-Ag alloys in artificial saliva solutions. Dent. Mater. 25, 672–677. https://doi.org/10.1016/j.dental.2008.10.016.

Zhang, D.C., Yang, S., Wei, M., Mao, Y.F., Tan, C.G., Lin, J.G., 2012. Effect of Sn addition on the microstructure and superelasticity in Ti-Nb-Mo-Sn Alloys. J. Mech. Behav. Biomed. Mater. 13, 156–165. https://doi.org/10.1016/j.jmbbm.2012.04.017.

Zhang, E., Li, F., Wang, H., Liu, J., Wang, C., Li, M., Yang, K., 2013. A new antibacterial titanium-copper sintered alloy: preparation and antibacterial property. Mater. Sci. Eng. C. https://doi.org/10.1016/j.msec.2013.06.016.

Zhang, L.B., Wang, K.Z., Xu, L.J., Xiao, S.L., Chen, Y.Y., 2015. Effect of Nb addition on microstructure, mechanical properties and castability of β-type Ti-Mo alloys. Trans. Nonferrous Met. Soc. China (English Ed. 25, 2214–2220. https://doi.org/10.1016/S1003-6326(15)63834-1.

Zhang, E., Wang, X., Chen, M., Hou, B., 2016. Effect of the existing form of Cu element on the mechanical properties, bio-corrosion and antibacterial properties of Ti-Cu alloys for biomedical application. Mater. Sci. Eng. C 69, 1210–1221. https://doi.org/10.1016/j.msec.2016.08.033.

Zhang, L., Guo, J., Yan, T., Han, Y., 2018. Fibroblast responses and antibacterial activity of Cu and Zn co-doped TiO 2 for percutaneous implants. Appl. Surf. Sci. 434, 633–642. https://doi.org/10.1016/j.apsusc.2017.10.169.